

ROLE OF PLASMA TEMPERATURE AND RESIDENCE TIME IN STAGNATION

PLASMA SYNTHESIS OF c -BN NANOPOWDERS

by

JONATHAN M DOYLE

A Thesis submitted to the

Graduate School-New Brunswick

Rutgers, The State University of New Jersey

in partial fulfillment of the requirements

for the degree of

Master of Science

Graduate Program in Mechanical and Aerospace Engineering

written under the direction of

Professor Stephen Tse

and approved by

New Brunswick, New Jersey

January, 2013

ABSTRACT OF THE THESIS

Role of Plasma Temperature and Residence Time in Stagnation Plasma Synthesis of c-
BN Nanopowders

By JONATHAN M DOYLE

Thesis Director:
Professor Stephen D. Tse

The synthesis of cubic boron nitride (c-BN) nanoparticles is examined experimentally by introducing borane ammonia precursor into a thermal plasma oriented in a stagnation point geometry, where nanoparticles are formed in the flow field upon reaching a cold substrate. The quasi-one dimensional flow field allows for correlating the plasma temperature and residence time to the final particle phase, morphology, size, and purity. Constant temperature and residence time cases are studied to assess the parameter's affect on the resulting particle characteristics. The as-synthesized nanoparticles are characterized by high-resolution transmission electron microscopy (HRTEM) and x-ray diffraction (XRD).

Cubic structured particles are synthesized at plasma temperatures of 3000-8000K and precursor decomposition times ≥ 0.030 s. The highest purity samples are produced at a plasma temperature and residence time of 6500K and 0.075s, respectively. Samples with lower c-BN content are observed with higher percentages of hexagonal and amorphous phases. The particle morphology shifts from spherical agglomerates to faceted shapes as c-BN purity increases. Also, particle size undergoes an increase in nominal size. The resulting phase and purity is proposed to be governed by growth

mechanisms that result in high-energy particle-particle interactions where the energy transferred is sufficient for atomic re-alignment into a denser phase.

Acknowledgements

I would like to thank Professor Stephen Tse for his guidance and mentorship. This work would not have been possible without him. Special thanks are given to my committee members, Profs. J. Shan and Z. Guo for their time spent editing this work.

Financial support for this project was provided by the Army Research Office (Grants W911NF-07-1-0644 and W911NF-08-0417), Office of Naval Research (Grant N00014-08-1-1029), and the New Jersey Space Grant Consortium.

Finally, this thesis is dedicated to my family for all their love and support.

Table of Contents

Abstract of the Thesis	ii
Acknowledgements	iv
Chapter 1.....	1
Introduction.....	1
1.1 Motivation, Objective and Strategies.....	1
1.2 Overview.....	3
1.3 Outline of Thesis.....	4
Chapter 2.....	5
Literature Review.....	5
2.1 An Introduction to Gas Phase Synthesis of Nanoparticles.....	5
2.2 Cubic Boron Nitride Synthesis	6
2.2.1 Effects of Ion Bombardment.....	6
2.2.2 Effects of substrate temperature.....	10
2.2.3 Effects of voltage bias.....	11
2.2.4 Effects of gas composition.....	11
2.2.5 Characterization	14
Chapter 3.....	17
Experimental Setup.....	17
3.1 Plasma Synthesis Configuration	18
3.1.1 Inductively Coupled Plasma Torch.....	18
3.1.2 Plasma Establishment	19
3.1.3 Gas Delivery System.....	21
3.1.4 Precursor Delivery Unit	23
3.1.5 Water-Cooled Substrate	24
3.1.6 Pressure Control System	25
3.1.7 RF Generator.....	26
3.1.8 Matching Network	27
3.1.9 RF coil.....	28
3.1.10 Synthesis Chamber.....	29
3.2 Operating parameters and procedure	30
3.3 Precursor Selection and Calculation of Precursor-Loading Rate.....	31

3.4 <i>Ex-situ</i> characterization methods	34
3.4.1 X-Ray Diffraction (XRD)	34
3.4.2 Transmission Electron Microscopy (TEM)	35
Chapter 4.....	37
Experimental Background	37
4.1 Experimental Parameters	37
4.2 Plasma Physics.....	38
4.2.1 Molecular Collisions	38
4.2.2 Dusty Plasmas	39
4.3 Heat Transfer Analysis	45
4.3.1 Plasma Gas Analysis.....	45
4.4 Flow Field Analysis	47
4.4.1 Stagnation Flow	47
4.4.2 Development of the Boundary Layer.....	49
4.5 Energy Analysis (Convection).....	50
4.6 Species Concentration.....	51
Chapter 5.....	52
Synthesis of Cubic Boron Nitride	52
5.1 Temperature Effect	52
5.1.1 Parameter Space.....	52
5.1.2 Results and Discussion	53
5.2 Residence Time Effect.....	60
5.2.1 Parameter Space.....	60
5.2.2 Results and Discussion	61
Chapter 6.....	69
Concluding Remarks.....	69
6.1 Review of Results	69
6.2 Future Work.....	70
References.....	72

List of Illustrations

Figure 1.1 Schematic of the experimental process.	3
Figure 3.1 Image of plasma synthesis reactor.	18
Figure 3.2 ICP Torch	19
Figure 3.3 Plasma synthesis setup.	20
Figure 3.4 Plasma generated by a 40.56MHz ICP.	21
Figure 3.5 Pictures of MFCs used in experiment.....	22
Figure 3.6 Screen image of LabView program used to control MFCs.	22
Figure 3.7 Precursor bubbler design.	24
Figure 3.8 Aluminum substrate used to collect as-synthesized nano-particles.....	25
Figure 3.9 1.5kW RF generator supplied by RF VII, Inc.	27
Figure 3.10 Impedance matching network.....	28
Figure 3.11 Gold varian RF coil.	29
Figure 3.12 Plasma synthesis chamber.	30
Figure 3.13 X-ray diffraction schematic.	35
Figure 3.14 TOPCON 002B TEM.	36
Figure 4.1 Image showing the axial symmetric temperature gradient within the flow approaching the substrate.	50
Figure 5.1 Plot of the percentage of cubic phase as a function of plasma temperature for different residence times.....	54
Figure 5.2 XRD and TEM of powder synthesized from an ICP at 4000K and 0.065s.....	57
Figure 5.3 (a) HRTEM and (b) TEM images (c) XRD of c-BN particles formed from a plasma temperature of 6500K.	58
Figure 5.4 TEM diffraction patterns of (a) amorphous and (b) a hexagonal/cubic boron nitride mixture.	59
Figure 5.5 TEM image and diffraction pattern of c-BN particles synthesized at a plasma temperature of 7500K and a decomposition time of 0.075s.	59
Figure 5.6 Percent cubic phase as a function of residence time.....	61
Figure 5.7 XRD spectrum of a c-BN/h-BN powder composition synthesized at 0.04s and 5000K.....	62
Figure 5.8 (a) Highly agglomerated hexagonal structured nano-particle (b) Hexagonal structure diffraction pattern.....	63
Figure 5.9 (a) Crystal growth from amorphous particle to h-BN (b) Onset of c-BN growth to increasing c-BN content (c) Nano-powders with majority c-BN content (d) Powders with >80% cubic phase.....	65
Figure 5.10 XRD of as-synthesized nanopowders formed at 0.075s and 7500K.	67
Figure 5.11 (a) TEM image and (b) diffraction pattern of the 0.075s and 7500K case.	67
Figure 5.12 (a) and (b) HRTEM images and (c) diffraction pattern of c-BN particles synthesized at a plasma temperature of 6500K and a residence time of 0.075s.....	68

List of Tables

Table 3.1 MFC data.	22
Table 3.2 Gas qualities.	22

Chapter 1

Introduction

The focus of this work is to determine the effects of temperature and residence time have on producing B-C-N nanostructures, including cubic boron nitride (c-BN). Investigation of fixed temperature and residence time cases on particle characteristics (such as morphology, crystallinity, purity, and size) are conducted.

Within this chapter, the motivation and objectives of this dissertation as well as the strategies utilized are presented. An outline of the ensuing chapters is also given.

1.1 Motivation, Objective and Strategies

B-C-N structures have been produced by several techniques such as plasma enhanced chemical vapor deposition (PE-CVD), electron beam epitaxy, arc discharge, and many other ion bombardment techniques, as well as high pressure-high temperature anvil techniques. Many groups have explored the growth mechanisms of these unique structures, but the results are inconsistent from case to case and phase diagrams are scarce. Production of boron nitride is done on large scales commercially, but the techniques utilized produce powders on the micron scale. Plasma synthesis can afford an environment without oxidizer, which may be advantageous for producing such nitride powders. A comprehensive fundamental study should encompass control over primary processing parameters that determine the resultant composition, phase, and mean primary and agglomerate particle size. The stagnation-flow geometry using an inductively-coupled plasma is strategically designed to allow for well-defined particle trajectories

through the flow field, and well as in-situ probing of the gas-phase flow field for velocity and temperature distribution, and species concentration distribution. Such information is important in scaling up reactors to accomplish commercial production of these materials.

To understand the growth mechanisms/conditions of synthesizing B-C-N structures, parametric studies are conducted to relate synthesis temperature and residence time to the purity and particle size of the resulting powder. Varying residence time at fixed plasma temperature helps to deduce the role of decomposition time on particle densification, i.e. transition through less dense phases into the desired more dense phase (cubic). Varying plasma temperature for fixed residence time helps to determine the role of synthesis temperature on powder purity. The resulting data can be helpful in developing a phase diagram for c-BN. The inductively-coupled plasma in stagnation flow can be considered quasi-one dimensional, where the only gradients are in the axial direction. This setup allows for determination of temperature, species concentration, and velocity distributions. These distributions can be measured by laser-based diagnostic techniques, such as Raman spectroscopy and laser-induced fluorescence (LIF), from which the results can be implemented to tailor the experimental parameters.

The main objectives of this work is to investigate as the roles of synthesis temperature and residence time in the gas-phase synthesis of B-C-N nanostructured powders to deduce fundamental growth mechanisms, using an inductively coupled plasma in an aerodynamically well-defined configuration. Some advantages of this process are: high degree of supersaturation, high quenching rate, and ability to produce non-oxide powders. The plasma provides the elevated enthalpy for decomposition of the

precursor, as well as the necessary energy to promote molecular kinetics for the desired chemical reactions to occur.

1.2 Overview

In this work, cubic boron nitride (c-BN) nanopowders are produced, and synthesis parameters are analyzed/optimized by iteratively employing the method shown in Figure 1.1.

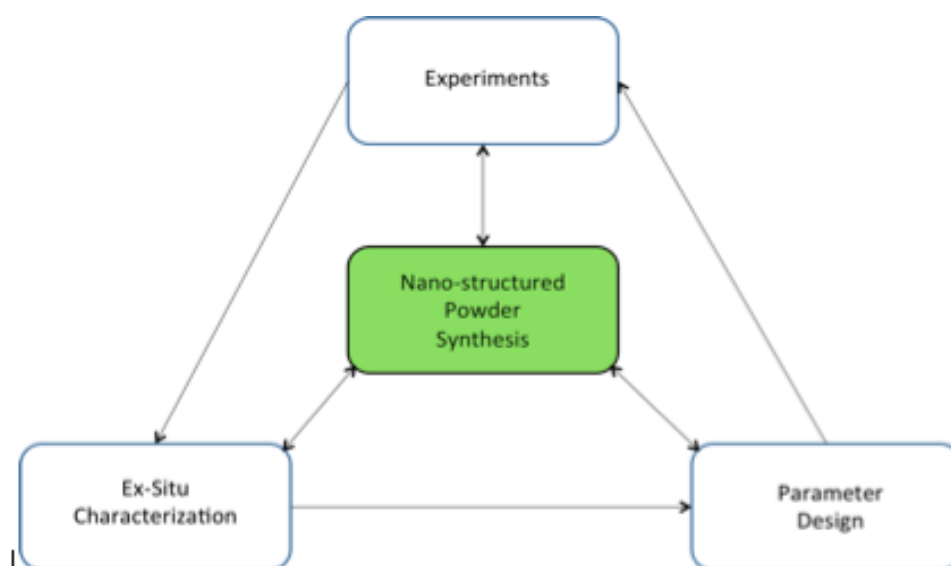


Figure 1.1 Schematic of the experimental process.

First, initial calculations of the bulk flow and boundary layer are made using the energy and diffusion equations to determine the extreme limits of the operational parameters, and to develop the experimental parameter space in-between. The extreme cases are conducted to give a baseline for the experiments to follow. Resulting powders are then characterized by X-ray diffraction (XRD) for composition and transmission electron microscopy (TEM) to analyze the as-synthesized particle size and morphology.

The experimental matrix identifies the synthesis conditions where the highest purity sample and smallest particle sizes are achieved.

Cubic boron nitride (c-BN) powders of various purities are synthesized by plasma temperatures between 3,000 and 8,500K, while using a single source precursor, i.e. borane ammonia. Residence time is adjusted from 0.005 to 0.08s. From this study percent cubic phase is plotted as functions of temperature and residence time. The resulting purities range from 0% to ~91%.

1.3 Outline of Thesis

Chapter 2 gives a comprehensive literature review of traditional synthesis methods for the production of the aforementioned material. Chapter 3 describes the experimental setups and procedures associated with the investigation of plasma synthesis of B-C-N nanopowders. Chapter 4 presents the plasma structure and governing equations. Chapter 5 examines the synthesis of cubic boron nitride nanoparticles, and the temperatures and residence times required for growth. Finally, Chapter 6 presents conclusions and remarks on future work.

Chapter 2

Literature Review

2.1 An Introduction to Gas Phase Synthesis of Nanoparticles

In gas phase synthesis of nanoparticles, conditions are created such that the vapor phase mixture is thermodynamically unstable relative to the formation of the solid material existing in nanoparticulate form resulting in a supersaturated vapor. Chemical supersaturation is reached when conditions are thermodynamically favorable for the vapor phase molecules to chemically react to form a condensed phase. If the degree of supersaturation is sufficient and the reaction/condensation kinetics is favorable, particles will nucleate homogeneously. Homogeneous nucleation is the formation of a new phase, either solid or liquid, without the aid of any foreign surfaces. Once nucleation occurs, remaining supersaturation can be relieved through condensation or surface reaction of the vapor phase molecules on the existing particles, and particle growth will occur.

1

Particle growth can occur by physical condensation of vapor onto particles, by chemical reaction on the particle surface, or by diffusion of the reactant into a particle followed by reaction within the bulk particle. Particle evolution (growth and morphology) involves four main mechanisms: (1) sintering (or coalescence), which is the fusing of two or more particles to form a single spherical particle—the mechanism by which an aggregate particle will reduce its surface area over time while retaining all of its mass; (2) coagulation, which is the collision between two or more particles to make one

larger particle that does not completely coalesce; (3) particle inception, which is the addition of new mass from the gas phase in the form of a monomer particle; and (4) surface growth, which is the addition of new mass from the gas phase directly onto the surface of an existing particle.

Therefore, in order to synthesize small particles, one needs to create a high degree of supersaturation by inducing a high monomer/cluster density, and then immediately quenching the system, so that the particles have limited particle growth and/or agglomeration. One useful way to classify synthesis methods is by considering the phase of the precursor and the source of energy used to achieve a state of supersaturation. Cubic boron nitride has been formed by several different techniques in the gas phase, all of which are based off of ion bombardment.

2.2 Cubic Boron Nitride Synthesis

The main obstacle in c-BN production is suppression of the hexagonal phase and amorphous structures. McKenzie et al.'s⁶ compressive stress model has shown that the deposition of c-BN is formed subsequently by an initial amorphous boron nitride sub-layer (a-BN) and a hexagonal buffer-layer. Ion beam assisted evaporation deposition (IBAED) has also shown promise due to quenching rates on the order of 10^{12} - 10^{14} K s⁻¹, which enables the material to be frozen into a metastable state.²

2.2.1 Effects of Ion Bombardment

Cubic boron nitride (c-BN) is similar to diamond-like carbon (DLC), such that it has sp³ hybridization. This leads researchers to believe that the synthesis techniques

should be similar for deposition of c-BN and DLC, which are heavily ion dependent techniques, such as plasma deposition, ion plating, magnetron sputtering, plasma enhanced chemical vapor deposition (PECVD) and electron beam epitaxy. In these techniques, c-BN needs a high flux ratio of energetic ions to neutrals for efficient deposition.³ But, found in other studies, any excess quantities of argon or nitrogen ions will cause the energy to become closer to the resputtering limit.⁴ Chowdhury and Pal⁵ have found that excess ion energy will not only cause resputtering, but also create conditions for transformation of sp^3 bonded-BN to sp^2 bonded-BN. McKenzie et al.⁶ has presented a critical compressive stress model based off of sub-plantation, which in the energy range of thin film technology, ions loose energy by nuclear stopping and elastic collisions with target atoms. The higher energy ions penetrate, via direct entry or knock on, and increase the density of the interstitial positions. Lower energy species, however, stick to the outer surface and form sp^2 bonded sites. A thermal spike is seen for a very short time span due to the remaining dissipating energy. The duration of the thermal spike is what ultimately governs the resulting phase, for example, amorphous films form during long thermal spikes. Robertson⁷ has also established c-BN is most efficiently formed by knock-on at higher energies, but below the resputtering limit.

Many researchers have experimentally determined how the ratio of cubic to hexagonal phases could be influenced by the ion current density impinging the substrate, which coincided well with McKenzie's compressive stress model. This is evident by an exponential relationship of the c-BN:h-BN with respect to the ion current density until an ion current density of 0.30 mA cm^{-2} , and is followed by a linear decrease believed to be the result of the energy approaching the resputtering limit. The ion current density can be

decreased by adding nitrogen into the flow to prohibit the occurrence of resputtering, which has been shown by Dworschak et al⁸ during the aforementioned study.

The energetic impact of ions on the substrate creates atomic mobility, which the resulting phase will depend on the mobility duration. McKenzie et al.⁶ discussed how mobility on the order of picoseconds will result in amorphous boron nitride films. Due to the induced compressive stress, a transformation from h-BN to r-BN, an unstable intermediate, to c-BN is created by causing the hexagonal sheets to move towards each other along the c-axis and changing the orientation to parallel which is preferential for the cubic structure.⁹

The compressive stresses formed by ion bombardment limit the film thickness, which has been shown by Hofsäss et al.¹⁰ where thicknesses of ~60-100nm were developed. During film growth from ion bombardment dependent processes, there is poor crystallinity and small grain sizes, along with delamination from the substrate. Films synthesized from supersonic plasma flows also created ion bombardment, in which created stress that induced cracking and delamination from the substrate.¹¹ Larsson¹² proposed a more “gentle” CVD technique to grow c-BN by avoiding bombarding ions that destroy the BN structure through surface penetration. Plasma assisted CVD techniques operate at relatively low energy regimes that will not penetrate the surface. This process is governed by diffusion of the B and N containing precursors and relies on self-assembly of the atoms. Bartl et al.¹³ hypothesized necessary conditions for c-BN growth in CVD processes as:

- 1) Stabilization of the c-BN surface during growth;
- 2) Sufficiently high mobility of the precursor material;

- 3) Preferential etching of h-BN and other non-c-BN phases; and
- 4) Preventing secondary nucleation of h-BN during c-BN growth.

To control these factors, one must understand vacancy generation, adsorption of growth species, and surface migration at the molecular level. In an ion vapor deposition (IVD) process, acceleration energies from 0.2-2keV were used to deposit B^+ and N^+ ions onto Si (100) wafers in B/N ratios from 1-5.¹⁴ The c-BN content increased with ion current density, but a maximum was seen at approximately 1keV.¹⁴ A DC arc plasma jet CVD was used to decompose a BF_3 -He- N_2 - H_2 gas mixture created a low-pressure, low-ion current density environment for non-stress induced c-BN growth. Grain sizes greater than 0.2 μ m were produced in films of approximately 20 μ m thickness.¹⁵

Another very interesting result, which enlightens whether ion bombardment processes truly produce the various phases of BN as layers building on top of each other, are nucleation experiments conducted by Ye and Oechsner.¹⁶ Films were synthesized using RF magnetron sputtering with variations on the experiment duration to capture the nucleation and growth process.¹⁶ From these results, h-BN tended to nucleate rapidly until a few minutes after deposition began and c-BN formation begins to develop. By investigating the B K-shell under irradiation, the π^* feature starts to diminish during the period of increasing c-BN growth. This means there is a physical transformation of h-BN to c-BN during deposition. To further confirm this phenomenon, the authors determined the volume of the films as a function of time. This revealed volume shrinkage during this period, which confirms the transformation from the less dense hexagonal phase to the denser cubic phase.

2.2.2 Effects of substrate temperature

Studies by Dworschak et al.⁶ have shown the necessary temperature increases come from thermal spikes by producing c-BN at ambient substrate temperatures. The substrate temperature was varied from 20°-450°C, and the c-BN content was found to increase continuously with increasing the substrate temperature. Higher substrate temperatures are believed to release the embedded hydrogen in the films, leading to higher density.⁶ At relatively low substrate temperatures, less than 75°C, all ion energies will induce amorphous boron nitride.⁷ The cubic phase will be formed with temperatures above 150°C, along with ion energy greater than 100eV. McKenzie et al.⁶ theorize the region around 227-327°C would be optimal for c-BN formation and smaller grain sizes. During an IBAED process, Kester and Messier¹⁷ found the dominant phase transition to occur at 300°C. Experiments conducted by Chowdhury and Pal⁵ used substrate temperatures slightly higher than the optimal range theorized by McKenzie et al.⁶, which may be due to the lack of substrate bias, and will be discussed later. Their optimal condition was found to be a substrate temperature of 350°C, which produced ~98% c-BN. Uchida et al.¹⁴ used a substrate at room temperature during an IVD process. The substrate was rotated to prevent unwanted localized heating and to create a uniform temperature distribution. The resulting powders had thicknesses up to 1µm, which may be due to the new substrate configuration. In a process where ion bombardment is not inducing c-BN growth, the substrate is heated to temperatures of 750-1050°C, which resulted in significantly less c-BN content compared to Chowdhury and Pal's¹² experiments, but ultimately proved that ion bombardment is not needed to synthesize the cubic structure.

2.2.3 Effects of voltage bias

Voltage bias has been used for years in hopes of creating an environment appropriate for growing substances. It has been shown by Dworschak et al.⁸ that the optimal c-BN growth condition is at a voltage bias of 650V. Their group has also shown that at 500V, there is only the hexagonal phase. This was explained by the bias being enough to change the preferred orientation of h-BN from c-axis perpendicular to parallel with respect to the substrate. Negative bias variations from -150V to -425V were used by McKenzie et al.⁶ to successfully develop c-BN films, but minimal content was developed at -150V. Oscillation of the voltage bias has enabled their group to grow the cubic phase at lower voltages. Murakawa and Watanabe¹⁸ used thermal plasma where the substrate bias was coupled in relation to the substrate and injector nozzle. This bias was increased linearly with an increase in substrate gap distance, but is extremely low compared to voltages used elsewhere. The resulting powders were poor in c-BN content. For Yamamoto et al.'s¹² low-pressure ICP system the voltage bias was inversely proportional to the substrate temperature, where the optimal condition occurred at -30V, resulting in ~80% c-BN.

2.2.4 Effects of gas composition

Many various techniques of incorporating the appropriate amount of boron and nitrogen into the gas mixture have been implemented. Dual sources, such as diborane (B_2H_6), pentaborane (B_5H_{15}), decaborane ($B_{10}H_{18}$) and boron fluoride (BF_3), along with nitrogen gas, have been popular alternatives for c-BN production. Dworschak et al.⁸ utilized a 10% B_2H_6 in argon mixture along with the appropriate nitrogen amount to achieve a boron to nitrogen ratio of 1:1. Yamamoto et al.¹⁵ utilized BF_3 as a precursor,

but later found B_2H_6 gave smaller particles along with higher c-BN content at lower temperatures, for reasons that will be discussed later.¹² Researchers⁸ have found hydrogen and helium gas to lower the c-BN content in chemical vapor deposition (CVD) thin film processes. Yoshida¹⁹ explicitly has shown that H and NH_x radicals are detrimental to c-BN deposition by finding a significant decrease in c-BN content with the existence of those radicals. This is in contrary to a paper published by Konyashin et al.²⁰ where excess hydrogen was determined to induce c-BN growth without a substrate bias. This may drive one to investigate the relationship between hydrogen content and substrate bias on the c-BN content of films developed by physical vapor deposition (PVD) and CVD. Chowdhury and Pal⁵ conducted experiments with floating substrate bias and a hydrogen rich precursor, borane ammonia (BH_3NH_3). Films with c-BN content exceeding 90% were readily produced with grain sizes of ~100nm. Dworschak et al.⁸ also discovered an optimum B_2H_6 precursor concentration, which gave a c-BN content of ~85%. Many gases such as hydrogen, fluorine, chlorine and bromine have been investigated for surface stabilization for c-BN growth. H and F have adsorption energies of 431kJ mol^{-1} and 430kJ mol^{-1} , respectively, for CVD diamond growth. Due to the similar crystal lattice parameters, one may make the assumption that these gases will also stabilize/maintain the sp^3 configuration for c-BN growth. H and F are thought to etch h-BN sp^2 to c-BN sp^3 under H^* and F^* impact.²¹ Hydrogen gas works very similarly, as compared to diamond growth, on both the B-rich and N-rich planes of (111) c-BN, while fluorine has a much lower stabilizing effect on the N-rich planes. This is due to fluorine requiring more energy to be extracted from the lattice. For continuing the growth of c-BN (111), one must look into preferential adsorption of N-containing

adsorbates. In the (110) planes, NH and NH₂ species prefer B surface sites while the same B-containing species (BH and BH₂) prefer nitrogen sites.⁹ In Larsson's paper¹², ammonia and boron bromide precursors were also investigated and determined to risk N-N and B-B bonding.

A mass-separated ion beam deposition technique can be used to produce B⁺ and N⁺ ions separately from precursors such as boron oxide and nitrogen gas.⁷ A plasma ion source creates the ions, which are then separated by magnetic mass separation to guide the separate beams into a deposition chamber. This gives tunability of the gas composition to achieve B:N of 1:1.

A strong influence of the ratio of Ar to N₂, which has shown a window where c-BN is the dominant phase, has been looked at by many researchers. A nitrogen/argon mixture will give more interstitials and vacancies, along with a lower penetration depth for film growth. McKenzie et al.⁹ discovered argon-nitrogen ratios of 2.5-4.0 give a high content of c-BN while higher ratios reveal no c-BN film growth. Chowdhury and Pal⁵ used an optical emission spectroscopy (OES) technique to determine the species concentrations within their inductively coupled plasma chemical vapor deposition (ICP-CVD) system. A critical argon concentration for c-BN growth was determined in relation to the nitrogen concentration, which is Ar:N₂ of 1:1.2. An optimal composition of precursor to plasma gas was also established. BH₃NH₃:(N₂+Ar) of 1:11 is believed to create conditions where the ion bombardment and excess amount of hydrogen are nearly optimal for pure c-BN growth.⁵

Watanabe et al.²¹ utilized h-BN powder of approximately 10µm as a boron source for their thermal plasma system, which also used very high flow rates of Ar and N₂.

From the resulting XRD patterns, the particle size decreases with an increase in substrate distance and the c-BN content also increases, in contrast to widely accepted transport theories. This phenomenon is due to the residence time through the plasma being too short, resulting in incomplete decomposition of the initial h-BN agglomerates.

2.2.5 Characterization

Infra-red spectra of c-BN can be misleading due to several close peaks with both h-BN and various silicon oxides at 1050 cm^{-1} . Electron energy loss spectroscopy of the B K edge region is the most accurate diagnostic tool for detecting c-BN, as a pre-edge is shown for h-BN.⁸ The sp^3 bonding, which is found in the cubic phase, can be distinguished by absence of the π^* feature and excitation of a K shell electron to the σ^* anti-bonding level.

Raman spectroscopy is another technique, in which c-BN is difficult to characterize. The lattice has low light absorption resulting in poor Raman scattering, which hinders the use of any resonance conditions.²² Werminghaus et al.²³ performed an ex-situ measurement of c-BN powders using HeCd, Ar^+ and Kr^+ laser lines ranging from 441.6-647.1nm for excitation of the molecules. Their monochromator utilized fixed slits of $100\mu\text{m}$ with 3 to 1.5cm^{-1} spectral resolution. The sample stage is able to map the whole specimen due to a 100nm step width. Cubic boron nitride spectra showed peaks at 1304 cm^{-1} and 1055 cm^{-1} for the longitudinal optical and transverse optical excitations, respectively. The best signal intensity for the longitudinal and transverse optical excitations were supplied by the 482.5nm of the Kr^+ laser and 488.0nm of the Ar^+ laser, respectively. As particle size decreases, the peak intensities become lower and the full width at half maximum becomes larger, along with being shifted towards a lower wave

number.²⁸ For example, samples with grain sizes less than 100nm presented broad peaks at 1280cm^{-1} and 1040cm^{-1} for the longitudinal and transverse optical excitations. This is described by a contradictory theory to the idealized phonon-confinement model, which only phonons near the center of the Brillouin zone contribute to Raman spectrum; a real crystal has grain boundaries and defects leading to photon momentum uncertainty.

X-Ray Diffraction (XRD) patterns will vary from process to process due to the different lattice stresses that may be developed during synthesis. Processes that rely more on ion bombardment will result in a shift towards higher 2θ values. XRD of c-BN produced by ICP-CVD are at 2θ values of 43.5° , 50° , and 88° , which correspond to the (111), (200) and (311) planes, respectively.³

Fourier Transform Infra-red Spectroscopy (FTIR) on samples produced by ICP-CVD showed peaks at $\sim 1060\text{cm}^{-1}$, for the B-N bond stretching of c-BN; 1370cm^{-1} , corresponding to B-N bond stretching of h-BN; and $\sim 780\text{cm}^{-1}$, relating to B-N-B bond bending.⁵ FTIR signals, like Raman signals, will be translated to higher wavenumbers when the lattice contains an increased compressive stress as seen during films produced by ion bombardment techniques. Relative intensities will change with the deposition temperature due to a variation in ion species. FTIR of samples from Guo et al.'s plasma electrolysis experiment have given peaks for c-BN at 1075cm^{-1} , and E-BN at 453cm^{-1} , 802cm^{-1} , 946cm^{-1} , 1191cm^{-1} , 1399cm^{-1} and 1635cm^{-1} .²⁴ RF magnetron sputtering produced FTIR peaks of 1100cm^{-1} for transverse optical excitation of c-BN and 800cm^{-1} and 1390cm^{-1} , for h-BN out-of-plane and in-plane stretching, respectively.¹³ This is due to a significant increase in lattice compressive stresses.

X-Ray Photoelectron Spectroscopy (XPS) is prudent for detection of differences between adsorbates and impurities. This is done by irradiating the surface and simultaneously measuring the kinetic energy of electrons emitted.²⁵ From this technique, the bonding between elements can be determined.

Chapter 3

Experimental Setup

In this work, production of B-C-N nanostructured particles is carried out in an inert environment using an inductively coupled plasma impinging on a cold substrate at atmospheric pressure. The plasma is established by introducing an Ar/N₂/(B_xN_yC_z precursor) mixture into a plasma torch through which post-plasma products impinge onto a water-cooled substrate to form a stagnation point flow. The evaporated metal-organic precursor is introduced into the plasma, which decomposes and undergoes nucleation, growth, and quenching into nano-sized particles. The desired nanoparticles (e.g. c-BN) can be collected from the water-cooled substrate due to thermophoretic deposition. Controlling the operating pressure and plasma temperatures to significantly reduce the particle residence time and inter-particle collisions (e.g. c-BN to c-BN particle collisions), to reduce both aggregate and primary particle sizes are of main importance. The plasma geometry is tailored such that condensing particles throughout the radial direction will experience similar time/temperature histories, due to similar trajectories, that will inherently produce a narrower particle size distribution.

In this chapter, the experimental setup for the atmospheric-pressure inductively-coupled plasma is presented. The procedures for selection of proper precursors and calculation of the precursor-loading rate are also given. Finally, characterization methods of B-C-N tertiary nanoparticles applied in this work are described.

3.1 Plasma Synthesis Configuration

The experimental setup was designed and manufactured as shown in Fig. 3.1, as part of this thesis work. The system is composed of a RF generator, matching impedance network, RF coil, inductively couple plasma torch, plasma gas and precursor delivery unit, water-cooled substrate, pressure control system, and a synthesis chamber.

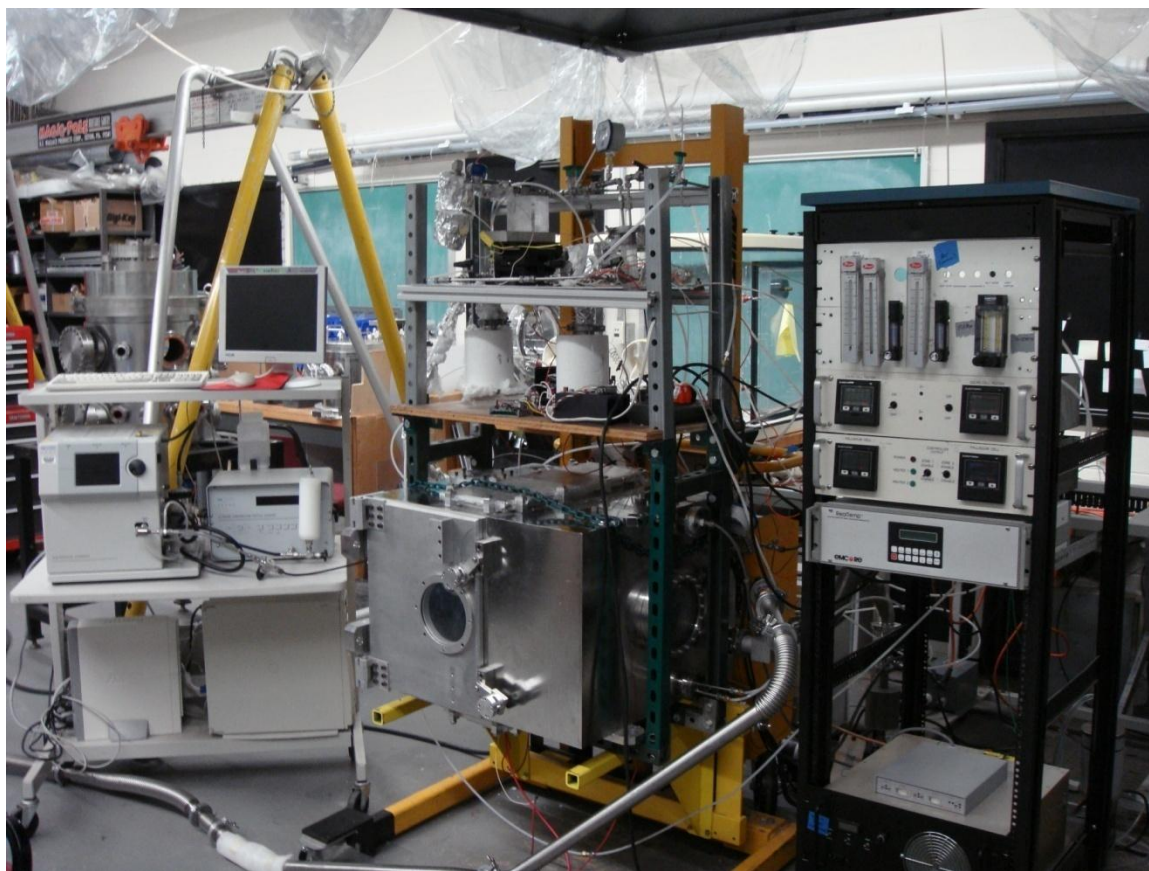


Figure 3.1 Image of plasma synthesis reactor.

3.1.1 Inductively Coupled Plasma Torch

The inductively coupled plasma torch is constructed from high temperature quartz and is comprised of three concentric tubes. The outer most tube is utilized for cooling the glass, in which case this flow is called the sheath gas. The plasma gas is introduced through the middle tube, which has an outer diameter of 15mm. A center injection

nozzle of 1.4mm diameter is implemented for precursor introduction. Plasma and sheath gas introduction are performed through inlets located tangentially to the flow, as shown in Figure 3.2, thus creating spiral trajectories to induce proper mixing (e.g. homogeneity of species concentrations).

The plasma torch faces down in the vertical direction, and is situated in a Teflon holder connected to mounting brackets. This bracket orients the torch perpendicular to the water-cooled substrate. A water-cooled substrate, supported by a scissor-jack, is placed downstream of the torch to form a stagnation point plane and consequently collect resulting powders. The distance between the torch and the substrate is adjustable.



Figure 3.2 ICP Torch.²⁶

3.1.2 Plasma Establishment

The axisymmetric, stagnation-point inductively coupled plasma (Fig. 3.3) is formed by flowing sheath and plasma gases, in our case the gases are both argon, then seeding with precursor vapor and nitrogen (or argon) gas through a radial inlet torch, onto

a water-cooled substrate. The RF generator is then set to a power, in which the gas mixture can be decomposed into ions. The plasma is ignited by a Tesla coil attached to the sheath gas inlet. This coil produces the free electrons needed to initiate the atomic excitation process. The RF generator and Tesla coil are simultaneously switched on to initiate the plasma, while the RF generator is the soul contributor to sustaining the plasma.

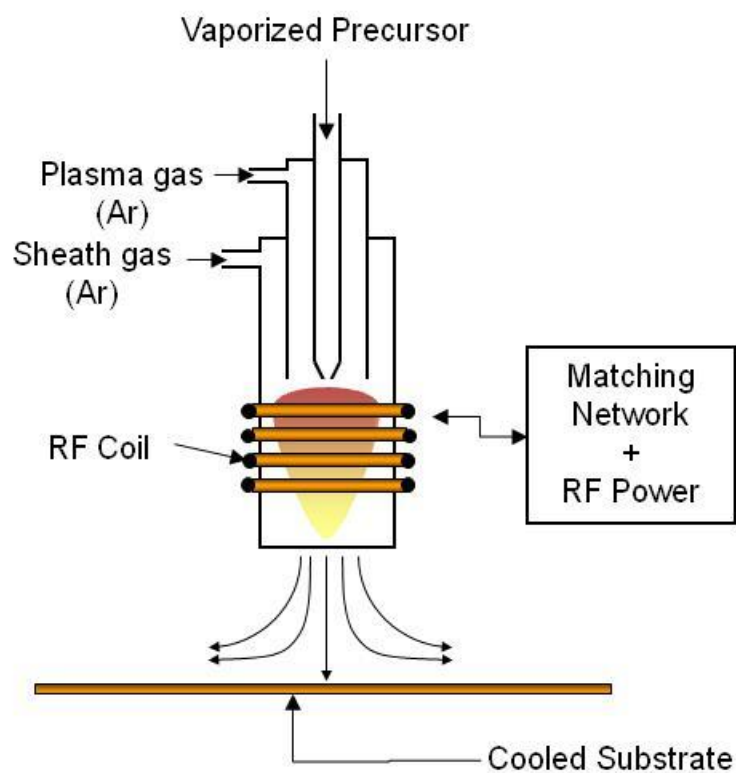


Figure 3.3 Plasma synthesis setup.

Solid powder-form precursors are sublimated and introduced into a carrier gas via a heater and temperature-controlled bubbling system, combined with an inert gas (i.e. N_2/Ar), and delivered to the injector nozzle within the torch. The precursor vapor pyrolyzes into ions that are nucleated in the post-plasma region into nanoparticles. Flows

are controlled and monitored with calibrated mass flow controllers (MFCs), rotometers, and the gas lines are temperature-controlled to prevent precursor condensation.

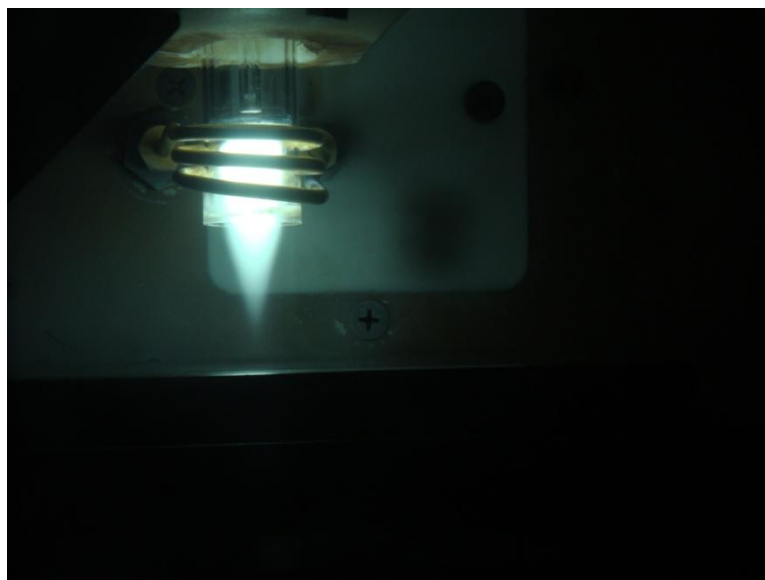


Figure 3.4 Plasma generated by a 40.56MHz ICP.

3.1.3 Gas Delivery System

The desired flow rate from the gas cylinders is controlled by mass flow controllers (MFCs) from Brooks Instruments. The ranges of flow rates for the MFCs used in this setup vary from 0-1 SLPM to 0-20 SLPM. The MFCs operate by a temperature difference, which generates a linear 0-5 V signal that is directly proportional to the mass flow rate of the gas. A LabView program with six outputs controls the appropriate mass flow rates, which allows the user to choose a flow rate set point as a percent of full scale for each MFC. MFCs are implemented to control the flow rate of the sheath and plasma gases. Terminating rotometers provide an insurance that the correct flow rates are being supplied to the system.



Figure 3.5 Pictures of MFCs used in experiment.

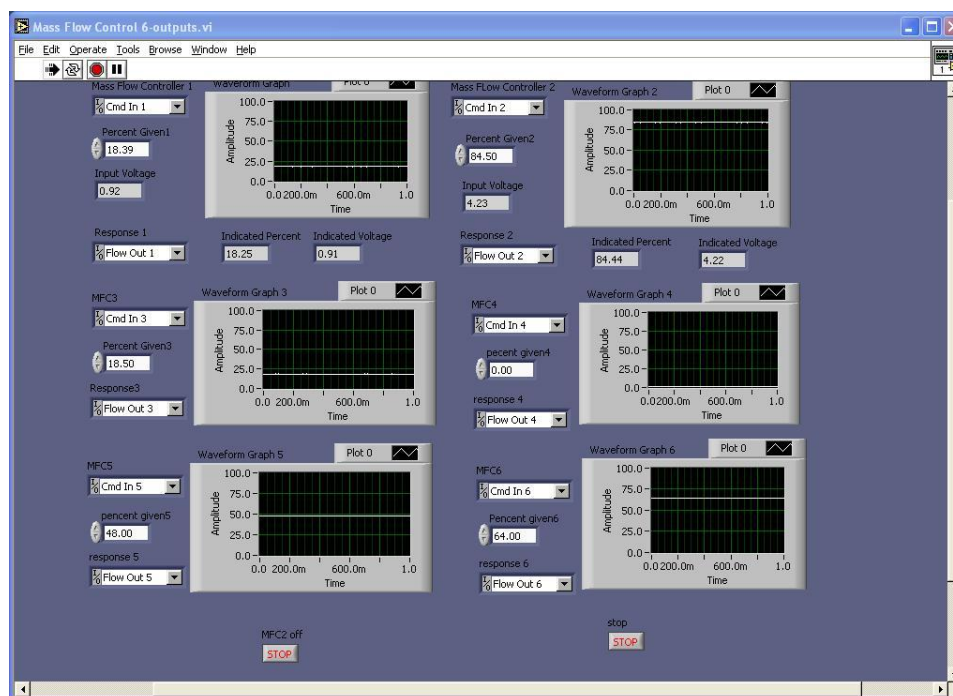


Figure 3.6 Screen image of LabView program used to control MFCs.

Below, Table 3.3, describes all of the MFCs with model numbers and flow rates implemented in the experiments. In Table 3.4, the gases along with the purity used are shown.

MFC	Model Number	Flow Rate Range (SLPM)
MFC 1	010011016727020	0-20
MFC 2	010040137591009	0-2
MFC 3	9812HC027899	0-1
MFC 4	9512HC030414	0-.5
MFC 5	9704HC035408	0-.1
MFC 6	9707HC030978	0-.1

Table 3.3 MFC data.

Gas	Purity
Argon (Ar)	Industrial Grade (97%)
Nitrogen (N ₂)	Industrial Grade (97%)

Table 3.4 Gas qualities.

3.1.4 Precursor Delivery Unit

Solid powder-form precursors (i.e. borane ammonia) are vaporized and introduced into a carrier gas (i.e. N₂/Ar) via a radiantly heated bubbling system. They are then injected into the center of the plasma region. N₂ gas is utilized as a carrier gas to sweep precursor vapor into the plasma for experiments where nitrogen is incorporated into the resulting powder's composition. A 3-inch-diameter ceramic circular heater is utilized to heat the bubbler. Insulated heating rope is wrapped around the stainless steel

(SS-316) tubing to act as a heating element. Temperature controllers are used in conjunction with K-type thermocouples, which are in direct contact with the tubing, to monitor and control the temperatures. The delivery lines are resistively heated and are usually set 50°C higher than the bubbler temperature in order to prevent precursor condensation. This bubbler system is illustrated in Fig. 3.7. Bypass 1 is kept closed during experiments and is only utilized when testing of the plasma system is necessary. Valves 3 and 2 are fully open prior to the plasma ignition; this is due to easier plasma tuning. The matching network uses an analog logic control to tune the plasma power for lowest reflection, which cannot compensate for a sudden influx of precursor vapor. For shutdown, valve 3 is closed followed by valve 2. Keeping any flow recirculation of the precursor material away from the MFCs is necessary to avoid contamination; thus this shut down order is very important.

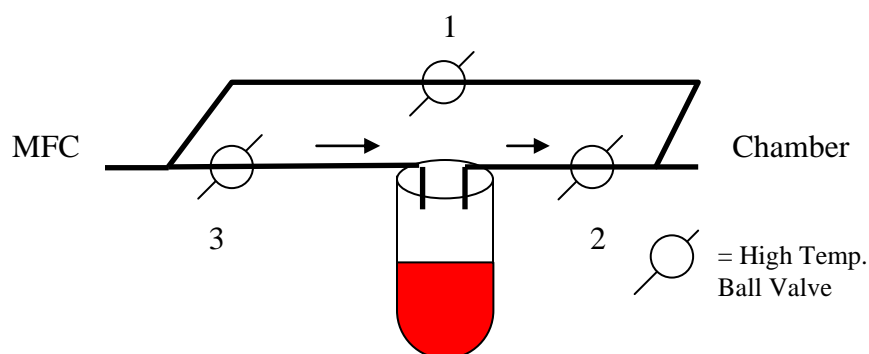


Figure 3.7 Precursor bubbler design.

3.1.5 Water-Cooled Substrate

In stagnation point geometry, a water-cooled substrate is placed directly below the inductively coupled plasma torch. A high temperature gradient is formed between the thermal plasma and the substrate to create nucleation of nanoparticles after the reaction

zone. The low temperature of the substrate also induces thermophoretic deposition of those nanoparticles. Water supplied to the substrate is delivered at a set point of 2°C for all experimental cases. Condensation is not a concern for these experiments, considering our reactor environment does not contain any water containing gases. Oxygen within our system would result in powder compositions far from the desired stoichiometry. Furthermore, any absorbed water species would create agglomeration during drying, which is undesirable in powder synthesis.



Figure 3.8 Aluminum substrate used to collect as-synthesized nano-particles.

3.1.6 Pressure Control System

The vacuum chamber is pumped down by a rotary vane vacuum pump, where the pressure is monitored by an absolute pressure gauge. This configuration is used to monitor and maintain the pressure to roughly ± 1 torr of the set-point pressure inside the synthesis chamber. A liquid nitrogen trap is designated between the pump and the

chamber to collect any harmful byproducts of the nanoparticle synthesis in order to protect the vacuum pump. Hard ceramic powders will damage the vacuum pump, thus removal of any particulates is prudent.

3.1.7 RF Generator

The radio frequency (RF) generator is manufactured by RF VII, Inc. and operates at 40.57MHz in a range of 0-1500W. Their generator was utilized over other manufacturers due to the higher signal to noise ratio compared to the competitors' units. The operation frequency gives the proper magnetic field skin depth to match the overall plasma torch diameter. The magnetic field skin depth is inversely proportional to the oscillation frequency.²⁷ The wide range of plasma power tuning available via this system allows our experimental temperatures to be varied significantly to tailor the nanoparticle nucleation and size.



Figure 3.9 1.5kW RF generator supplied by RF VII, Inc.

3.1.8 Matching Network

The matching network is a circuit of two adjustable capacitors, one for tuning and the other for supplying the load. The load capacitor is a Jennings (model no. GCS-100-7.5S) 5-100 picofarad 7.5kV vacuum capacitor, while the tuning is done by a MFJ Enterprises 3000W antenna tuner. These capacitors are driven by 12VDC motors produced by Coleman Motors Products, which are connected to 10-turn potentiometers that give feedback signals to the logic tuning box. This allows the system to optimize the plasma power for the given gas mixture flowing through the torch. The connected logic tuning box compensates for the impedance within the system, allowing efficient energy transfer.

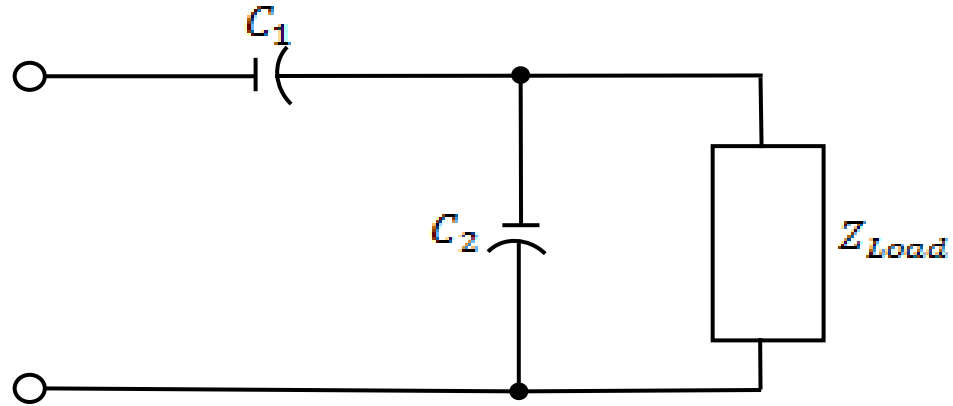


Figure 3.10 Impedance matching network.

3.1.9 RF coil

Several different coils were tested for optimization of the transmitted signal. Silver plated coils were found to transmit a noisier signal, thus producing less powerful plasma. Two variations of gold coils were considered, the first was a Varian series gold coil, and the second was a similar model also from the same manufacturer. The first gold coil orientated the plasma torch in too close proximity to the matching network, which created recirculation of product gas and thus hindered the stagnation point geometry. A modified version of the first gold coil was manufactured to prevent this occurrence. The final gold coil transmits a very clean signal to create plasma free of any reflected RF power.



Figure 3.11 Gold varian RF coil.

3.1.10 Synthesis Chamber

The synthesis chamber is constructed of 316-stainless steel with inner dimensions of 25"x24"x18" (LxWxH), as shown in Figure 3.12, whose inside pressure is maintained by the pressure control system. The pressure level in the chamber during experiments is kept at atmospheric conditions. Inside the chamber, the torch and substrate geometry is constructed as described in Section 3.1.1. The chamber is configured with three orthogonal fused silica viewports for optical access, and the entire chamber is mounted to a movable motorized lift to enable laser-based diagnostic spatial probing of the plasma temperature and flow field properties. The free electron producing Tesla coil transmits the high voltage through a non-resistive electrical feed-through via a chamber sidewall port. Two more electric feed-throughs are used to supply power for the insulated heating rope on the interior gas lines. The final electrical feed-throughs are for transmitting the RF signal to the matching network and for the tune control box to adjust the capacitors in order to match the system impedance.

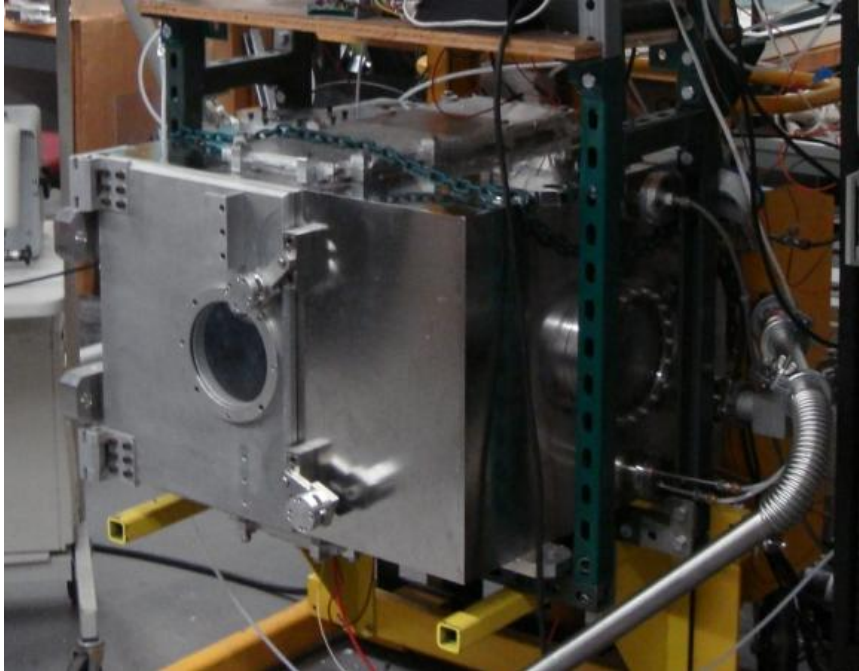


Figure 3.12 Plasma synthesis chamber.

3.2 Operating parameters and procedure

The plasma in this work use Ar and N₂ gases both of industrial grade from Airgas with minimal impurities such as oxygen. Precursor loading is varied between 1.214×10^{-4} and 3.19×10^{-4} g/s, and a substrate-torch-gap varies ranging from 2.54cm to 7.62cm.

The experimental procedures are given as follows:

- (1) Pump the chamber down, and check the chamber leakage rate;
- (2) Flow N₂/Ar (depending upon the desired product) into the chamber, and bring the pressure up to 1 atmosphere;
- (3) Open the valve immediately downstream of the bubbler to equalize the bubbler pressure with the chamber pressure

- (4) Turn on the temperature controller to bring the bubbler temperature to the set-point (140-180°C, depending upon desired precursor loading), as well as the other temperature controllers for the delivery lines (190-230°C);
- (5) Switch on the water baths, and bring the temperatures of the substrate and matching network to the set points (2 °C and 18 °C respectively);
- (6) Pour liquid nitrogen into the nitrogen trap to capture the condensable particles and to protect the vacuum pump from contamination;
- (7) When all of the temperatures (including the bubbler, lines, matching network and substrate) become stable, open the valve downstream of the bubbler;
- (8) Set the RF plasma power to ~500-1400W;
- (9) Open MFCs simultaneously;
- (10) Once the flow reaches steady state, spark the plasma;
- (11) Run the experiment for 10 minutes; then close the upstream valve; and close the downstream valve (to prevent contamination in the mass flow controller);
- (12) Close the nitrogen, while allowing the argon to flow for 15 minutes to vent precursor residue. Argon is chosen over N₂ because it will not absorb into the synthesized powders;
- (13) Turn off the vacuum pump.

3.3 Precursor Selection and Calculation of Precursor-Loading Rate

As stated by a previous lab mate, the precursor must be deliverable in vapor form, have a suitable vapor pressure, preferably be a liquid at room temperature, and have a volatilization temperature of 250°C or lower.¹ Precursors containing boron are seldom available in liquid form without containing oxygen, so powder-form compounds are

deemed suitable. Borane ammonia (BH_3NH_3) is selected to produce c-BN for the duration of this study. Its melting point is 93°C and the boiling point was experimentally determined to be 140°C under 1 atm of an inert environment. Heating within the presence of oxygen will cause the compound to react violently, so heat must only be applied after the bubbler system is flushed with an inert.

The vapor pressure of the precursor mentioned above can be determined by the Clausius-Clapeyron relation:

$$\ln(P_2) = \ln(P_1) - \frac{\Delta H_{vap}}{R} \left(\frac{1}{T_2} - \frac{1}{T_1} \right) \quad (3.1)$$

Carrier gas (Ar or N_2) is used to sweep the precursor vapor from the heated bubbler. This vapor is assumed to be completely saturated and exit the bubbler at a pressure, P_o , which is effectively the chamber pressure.

Bubbler temperature, bubbler pressure, and carrier gas flow rate affect the precursor transfer rate. The precursor-loading rate is calculated in the following manner:¹

$$F_r = \frac{F_c P_r}{P_o - P_r}, \quad (3.2)$$

where the variables are defined as

F_r : flow rate of the precursor vapor at the standard temperature and pressure (STP) in liters per minute (L/min)

F_c : flow rate of the carrier gas (set with the MFC) at STP in liters per minute (L/min)

P_o : downstream pressure immediately after the bubbler (each experiment was ran at a pressure of 1 atm)

P_r : thermodynamic vapor pressure of the precursor at a certain temperature (torr)

Equation 3.2 is accurate for precursor-loading flows with output pressures in the range $P_0 > 3P_r$. Therefore, the bubbler temperature is varied from case to case, based upon the desired precursor-loading rate.

The gaseous mixture is assumed to be consistent with ideal gas behavior, thus allowing the precursor-loading rate to be calculated as follows:

$$\text{Precursor – loading rate (mol/min)} = \frac{F_r(\text{L/min})}{22.4(\text{L/mol})}$$

(3.3)

The precursor level drops as the vapor leaves the bubbler, which if the liquid level drops below a certain depth the vapor will have insufficient time to fully saturate in the bubbler. Therefore a minimum precursor level should be maintained in the bubbler, for which during this work's experiments the level is kept above 2cm.

Via mass transfer of the precursor, the bubbler temperature fluctuates due to the particles on the surface being swept away. Instabilities in the bubbler temperature can be avoided by introducing N_2 into the bubbler before heating, balancing the pressure between the reactor and the bubbler.

Introduction of the precursor into the plasma can be visually determined by distinct color emission unique to each compound. The plasma initially has bright white emission from the argon emission at wavelengths throughout the spectrum: 351.1 nm, 363.8 nm, 454.6 nm, 457.9 nm, 465.8 nm, 476.5 nm, 488.0 nm, 496.5 nm, 501.7 nm, 514.5 nm, 528.7 nm, 1092.3 nm.

²⁸ Once the precursor is carried into the plasma, the various compounds emit light at ~530nm.

A transition in full RF load being transferred to the gaseous mixture occurs within the first 30 seconds of experiment startup. To avoid depositing particles in which the exact growth conditions are unknown, a plate is used to block deposition before steady state is reached. It is taken away after the plasma power becomes stable and precursor decomposition is uniform in the plasma. Only powders deposited during steady-state synthesis are collected and characterized.

3.4 *Ex-situ* characterization methods

Various techniques are used to characterize the as-synthesized particles to obtain the powder properties such as phase composition, crystallinity, morphology, aggregate particle size, and primary particle size.

3.4.1 X-Ray Diffraction (XRD)

The phase composition, which is the type and number of phases present, is identified by XRD. XRD checks for regular repetition of an arrangement of atoms or molecules over a distance much larger than the unit cell. Bragg's equation governs the X-rays diffracted by the crystalline phases, which relates the lattice spacing to the X-ray wavelength. Widths of the peaks are related to the crystal size by the Scherrer equation:

$$d = \frac{k \times \lambda}{FWHM \times \pi / 180 \times \cos \theta}, \quad (3.4)$$

where the variables are defined as

k : shape factor of the average crystallite (expected shape factor is varied upon the desired powder composition)

λ : wavelength (1.54056 Å for Cu K $_{\alpha}$)

θ : diffraction angle.

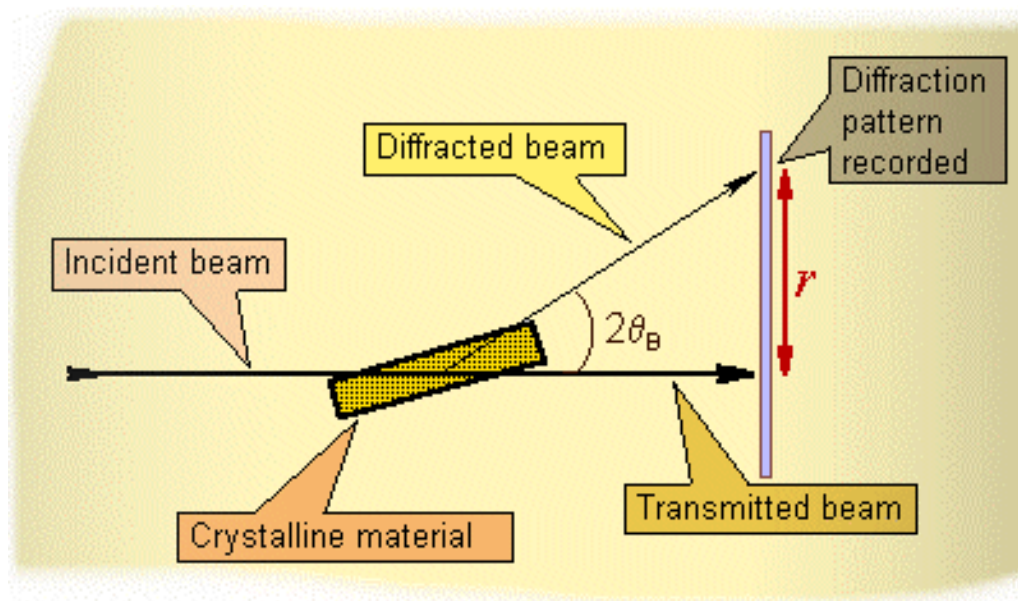


Figure 3.13 X-ray diffraction schematic.²⁹

Using quantitative analysis, the crystalline phase compositions, and amorphous phase, if any, can be obtained. In this study, we use XRD (Siemens D500 X-ray Diffractometer) to obtain the phase composition, crystallinity, and crystalline size of the as-synthesized nanoparticles.

3.4.2 Transmission Electron Microscopy (TEM)

Morphologies, grain sizes, and mean particle diameter of the synthesized nanoparticles are acquired by use of TEM (TOPCON 002B). The TOPCON 002B consists of a LaB6 gun and has the capability of an operating accelerating voltage of

200keV. High resolution TEM (HRTEM) can be used to evaluate the atomic-level structures of these particles. Selected area electron diffraction (SAED) is performed to evaluate the crystallinity and phase composition of individual $B_xC_yN_z$ nanoparticles.



Figure 3.14 TOPCON 002B TEM.³⁰

Chapter 4

Experimental Background

4.1 Experimental Parameters

Synthesis of c-BN nanoparticles is a complex function of primary adjustable parameters within the thermal plasma technique. The extrinsic parameters, residence time and plasma temperature, are manipulated by adjusting the intrinsic parameters. These parameters include carrier gas flow rate, total mass flow rate, and radio frequency power. The residence time is primarily affected by the total mass flow rate, while being a small function of RF power. Plasma temperature is a result of the RF power and mass flow rate, which can be estimated by means that will be discussed in the next section.

The total mass flow rate is adjusted by the MFCs, which are discussed in the previous chapter and can be adjusted between 0.2 and 0.6 g/s. The upper limit is due to the RF power, which more mass passing through the oscillating magnetic field will result in lower temperatures. For the experiments conducted in this study the RF power is adjusted between 500W and 1400W. To simplify and isolate the experiments to constant temperature and constant residence time, the various parameters were adjusted to meet the desired conditions.

4.2 Plasma Physics

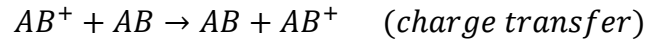
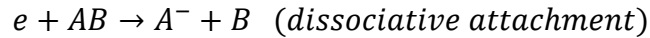
4.2.1 Molecular Collisions

Gas phase collisions within chemically reactive discharges include dissociation of molecules, generation and destruction of negative ions, and gas phase chemical reactions. The dissociation of molecules is the central role in the chemistry of reactive discharges at low-pressure. Hot neutral fragments are typically generated during this type of event because of the energy difference magnitude between the collision (kinetic energy) and the dissociation (latent heat).

Dissociation typically occurs due to collisions between electrons and the precursor molecule. The interaction time for the collision ($t_c \approx 10^{-16}$ - 10^{-15} s) is significantly short compared to the time required for the molecule to vibrate ($\tau_{\text{vib}} \approx 10^{-14}$ - 10^{-13} s). According to the Franck-Condon principle, the electron collisional excitation of a molecule to an excited electronics state, the new vibrational state can be determined by freezing the nuclear motions during the collision. This means excitation to an excited state will lead to dissociation when it is energetically permitted.

Collisions within reactive discharges are broken down into subgroups consisting of ionization, dissociative attachment, recombination, charge transfer and elastic scattering. Elastic scattering and charge transfer are considered ion-neutral momentum transfer collisions. This results in effective diffusion coefficients for positive and negative ion species. Monte Carlo methods are typically used for the collisional dynamics, which is based on a cross-section set. Also, generally there is no assumption of a Maxwellian electron distribution.





In low pressure discharges, the plasma is not in thermal equilibrium and electrical power is coupled most efficiently to plasma electrons. The supplied energy is transferred inefficiently from electrons to neutrals and ions. Dissociation and excitation processes can lead to relatively high-energy heavy particles, while ambipolar electric fields accelerate positive ions toward the sheath edge. Due to the low pressure, the electron number density is deficient resulting in the electron mean-free path being on the order of the discharge dimension. This observation yields ionization as the primary collision mode, which is seen with noble gas plasmas.

4.2.2 Dusty Plasmas

In etching and deposition processes, particulates can contaminate the final product. Dusty plasmas recently have been explored for powder synthesis and surface modification due to its unique particulate growth within the discharge. Probing the plasma shows the dust particle charges negatively with a potential several times the electron temperature. Numerous variations to the particle size, density, and energy will affect the potential and charge as follows:

1. Very energetic electrons will emit secondary electrons from the particle surface, which leads to lower potential and charge.
2. If the particles are larger in diameter with high density this leads to a larger particle charge than the electron charge density. An electronegative equilibrium

is developed in which the negative ions are the negatively charged dust particles, leading to more complicated plasma stratification.

3. When there is a sufficient density of dust grains, their Debye spheres will overlap resulting in a modified equilibrium. These plasmas are known as *strongly coupled plasmas* due to having more potential than kinetic energy.

These local phenomena lead to change in global discharge properties, such as the tendency for particulates to collect near processing discharge sheaths. This is due to the positive ion flow outward leading to an outward frictional force on the particulates, which balances the electric field force. In the plasma considered in this study, the positive ion friction force is dominant and results in the particulates being attracted to regions where the electric field force is larger.

Determination of the equilibrium potential and charge is imperative to understanding the plasma characteristics. A typical discharge consists of $T_e \gg T_i$; and the Debye length for shielding around an isolated charged sphere with $a \ll \lambda_D$ is $\lambda_D \approx \lambda_{Di} = (\epsilon_0 T_i / en_i)^{1/2}$. By orbital motion limited theory for a spherical probe and assuming an isotropic Maxwellian distribution for both electrons and ions, the currents are defined as:

$$I_{e0} = en_e \bar{v}_e \cdot \pi a^2$$

$$I_{i0} = \frac{1}{4} en_i \bar{v}_i \cdot 4\pi a^2$$

The particulates' potential is approximated analytically by Matsoukas and Russell as³¹

$$\Phi_d \approx -0.73 T_e \ln \left(\frac{M T_i n_e^2}{m T_e n_i^2} \right)^{1/2} .$$

To determine the charge build-up within a dust grain entering the plasma region with non-equilibrium initial conditions, one must numerically solve the following equation.

$$\frac{dQ}{dt} = -I_{e0} \exp\left(\frac{Q}{C_d T_e}\right) + I_{i0} \left(1 - \frac{Q}{C_d T_i}\right).$$

After solving the equation above, this results in obtaining an estimate for the charging time constant, shown in the equation below.

$$\tau \sim \frac{C_d T_e}{I_{e0}}.$$

In dusty plasmas, this time constant, which is on the order of μs , is typically short when compared to the dust particles' growth time. The distribution of charge number within dusty plasmas has been found to follow a Gaussian distribution for $Z \gg 1$ and $n_e \approx n_i$

$$f_d(Z) = \frac{1}{(2\pi\sigma_z^2)^{1/2}} \exp\left[-\frac{(Z-Z_d)^2}{2\sigma_z^2}\right],$$

where the standard deviation is defined as $\sigma_z \approx 0.5Z_d^{1/2}$.³² Experiments by Boufendi et al.³³ determined the charge number to be $Z_d \approx 477$, which would result in most of the plasma's negative charge residing from the particulates. Electrons are emitted from dust grains due to field emission, electron, ion and metastable impact, UV photon absorption, and thermionic emission. Spherical particles with radii less than 4nm do not experience particulate charge build up, while non-spherical particles can experience charge build up in particle sizes up to 10nm. Under high T_e , secondary emission due to electron impact becomes a significant fraction of the primary current. Another unique phenomenon due to secondary emission, in this case of UV photon absorption, will result in the dust becoming positively charged. This is seen in the implemented plasma within this work and is due to neutral excitation by electron impact. Past studies have shown that up to

50% of the plasma power can be transferred to UV resonance radiation in noble gas discharges. Within dusty plasmas, significant amounts of radiation can be reflected within the plasma region, creating a condition where the internal UV flux is much higher than the emitted radiation at the surface.

When determining equilibrium within dusty plasmas, one must acknowledge the electron number density will decrease with time resulting in higher electron temperatures. This effect is driven by particulate build up over time. This results in a particle balance in the volume between production due to ionization and the loss to the surroundings, i.e.,

$$K_{iz}n_en_gV = \Gamma_iA,$$

where Γ_i , V , and A are defined as the particle loss flux, volume, and discharge cross sectional area, respectively. The electron power balance is where the ohmic power equals the electron power losses and is shown in the below equation, i.e.

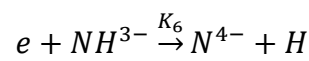
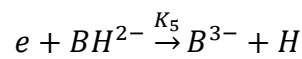
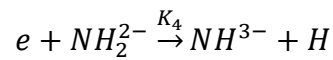
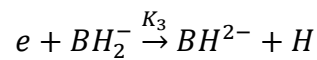
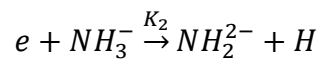
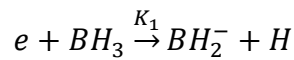
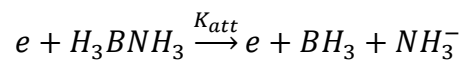
$$\frac{1}{2} \frac{j_{rf}^2}{\sigma_{ac}} V = \Gamma_i A e (\mathcal{E}_e + \mathcal{E}_c).$$

with σ_{ac} being the AC plasma conductivity; and $\mathcal{E}_e + \mathcal{E}_c$ being the electron energy lost per electron lost from the discharge.

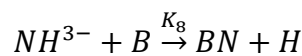
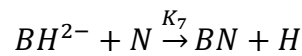
Formation and growth of dust grains is not fully understood thus far, leading to characterization by infrared absorption, mass spectroscopy, Raman spectroscopy, laser induced fluorescence, and other techniques. Hollenstein et al.³⁴ have observed negative ion clusters having masses up to 1300amu, which corresponds to 1.2nm diameter particles for the composition stated within their study. This shows that the precursors form microscopic dust grains in low pressure discharges from singly charged negative ion clusters. At low pressure, clusters form from feedstock dissociation fragments that combine with negatively-charged clusters. These negative clusters are confined to the

plasma region and are dominant over neutral cluster buildup, since the neutrals are lost due to diffusion. The clusters grow through coagulation when the number density is sufficiently large. Once coagulation of grains exceeds 10nm, the growth rate decreases due to buildup of negative charges. Slower accretion of mass by collisions with neutrals also results in smaller particle sizes.

An example for negative ion cluster formation in a plasma containing the precursor mentioned previously begins with dissociative attachments to strip the starting molecule down to its constituents. The possible dissociative reactions with the plasma are as follows:



The probability of one of these reactions to occur rather than the other is dependent upon the number density of a particular species.



The dissociative reactions are followed by a series of neutral insertion reactions, which lead to formation of boron nitride molecules. The neutrals can consist of vibrationally-

excited precursor or its dissociation fragments. When neutral clusters are formed, they are lost from the plasma region on a faster timescale resulting in smaller dust grains. Letting n_j be the density of the j th negative cluster, then accounting for production and loss by the insertion reaction and loss by recombination, we have the particle balance for the $(j+1)$ st cluster, i.e.,

$$\frac{dn_{j+1}}{dt} = K_j n_g n_j - K_{j+1} n_g n_{j+1} - K_{rec} n_{j+1} n_i, j = 1, 2, \dots$$

where n_g is the precursor number density. Once the number densities of the ionized, excited, etc. species are established, the number density of the particular dust grain of interest is found by solving

$$\frac{dn_d}{dt} = -K_{dd} n_d^2.$$

The solution of this equation leads to the Brownian free molecular motion for neutral coagulation and enables one to develop the variation in particle radii as a function of time, i.e.,

$$r(t) = r_0 \left(1 + \frac{5}{6} n_{d0}^{5/6} C t \right)^{2/5}.$$

This analysis of dusty plasmas lays the groundwork for the dissociation of the precursor leading to formation of the desired dust grains and eventually the particle growth evolution upon exiting the plasma region.

4.3 Heat Transfer Analysis

4.3.1 Plasma Gas Analysis

A simple convection analysis of the plasma torch will supply one with a rough estimate of the plasma temperature. From Newton's law of cooling, as shown in Equation set (4.1) this temperature can be found.

$$\dot{q} = \dot{m}c_p(T_o - T_i) \quad (4.1a)$$

$$T_o = T_i + \frac{\dot{q}}{\dot{m}c_p} \quad (4.1b)$$

For the constant temperature cases, the total mass flow rate needs to be calculated for various RF power levels. Rearranging Newton's cooling law to solve for the mass flow rate yields:

$$\dot{m} = \frac{\dot{q}}{c_p(T_2 - T_1)} \quad (4.2)$$

This will give the mass flow rate as a function of the plasma power for a constant temperature experiment series. To establish the user-adjustable parameters, calculation of the gas velocity at the exit is needed. First, the density variation with temperature must be determined as shown in Eqns. 4.3 and 4.4.

$$\beta = \frac{1}{V} \left(\frac{\partial V}{\partial T} \right)_{\square} = \frac{nR}{PV} = \frac{1}{T} \quad (4.3)$$

$$\rho_1 = \frac{\rho_o}{[1 + \beta(T_1 - T_o)]} \quad (4.4)$$

Where β is the coefficient of thermal expansion and has units of K^{-1} . Once the expanded density is established the volumetric flow rate at the exit can be calculated, which leads to an expression for the gas exit velocity.

$$\dot{v} = \frac{\dot{m}}{\rho_1} \quad (4.5)$$

$$u = \dot{v} \cdot \frac{1}{A} \quad (4.6)$$

From the expression for the exit velocity, u , the Reynolds number of the flow can be calculated to determine laminar or turbulent flow.

Applying mass conservation between the torch inlet and outlet gives the expression shown in Eq. 4.7. Also, assuming the specific heat of argon is a small function of temperature, the change in c_p throughout the torch length will be neglected and the mass conservation becomes:

$$\dot{m}_{in} = \dot{m}_{out} = \rho_{in @ 300K} \dot{v}_{cold} \quad (4.7)$$

The above equation results in a relationship for the inlet volumetric flow rate, which is the user input for controlling the inlet gas. From the above calculations, all aspects of the experiment regarding the plasma temperature and exit velocity can be determined where the latter is the main contributor to the particle residence time.

For the constant residence time cases, a particular duration from the plasma region to the cooled substrate is desired and all other experimental parameters must be developed from this value. The plasma gas exit velocity is evaluated by keeping the substrate distance constant throughout all cases conducted within this study and is shown in Eq. 4.8, i.e.

$$u_{exit} = h_{s-t} / t_{res}. \quad (4.8)$$

Through similar manipulation from the previous evaluation of the constant temperature case, the outlet volumetric flow can be determined.

$$\dot{v}_{out} = u_{exit} \cdot A_{torch}. \quad (4.9)$$

The determination of mass flow rate is done by the same as shown before, but the outlet density is found by an iterative method from the resulting outlet temperature. The outlet temperature is evaluated by Eq. 4.1b and is used to re-evaluate the outlet density. This calculation process is repeated until the difference between consecutive temperature calculations is within a specific tolerance.

4.4 Flow Field Analysis

4.4.1 Stagnation Flow

The experimental setup utilizes a stagnation point geometry that coupled with a uniform exit velocity allows one to simplify the flow field. At the stagnation point, the flow velocity slows to zero while no slip is considered on the substrate surface. The no slip condition allows for particles being carried in the flow field to adhere to the substrate. This flow is assumed laminar over the plate, thusly giving a radial uniform powder distribution. The continuity equation for this flow field geometry is

$$\frac{\partial(ru)}{\partial r} + r \frac{\partial(\rho v)}{\partial z} = 0, \quad (4.10)$$

and the radial momentum equation, using the assumption of a boundary layer becomes

$$u \frac{\partial u}{\partial r} + v \frac{\partial v}{\partial z} = -\frac{dp}{dr} + \mu \frac{\partial^2 u}{\partial z^2}. \quad (4.11)$$

The flow just outside of the boundary layer is assumed to be the free stream velocity, which varies as $U = C \cdot r$. Since r depends on x , a Mangler's coordinate transformation is performed to remove the dependence and is related to the original coordinate system by

$$\bar{x} = L^{-2} \int_0^x r^2(\square) dx, \quad (4.12)$$

$$\bar{z} = r(x)z/L, \quad (4.13)$$

where this transformation is valid within the regions where $d\bar{z} = (r/L)dz$ and $d\bar{x} = \left(r^2/L^2\right)dx$. From stream function analysis, the Cauchy-Riemann equations are determined as:

$$\frac{\partial\psi}{\partial z} = \frac{ru}{L}, \quad (4.14)$$

$$-\frac{\partial\psi}{\partial x} = \frac{rv}{L}. \quad (4.15)$$

Applying the coordinate transformation discussed above and substituting into the momentum equation gives

$$\frac{\partial\psi}{\partial\bar{z}} \frac{\partial^2\psi}{\partial\bar{x}\partial\bar{z}} - \frac{\partial\psi}{\partial\bar{x}} \frac{\partial^2\psi}{\partial\bar{z}^2} = U \frac{dU}{d\bar{x}} + \nu \frac{\partial^3\psi}{\partial\bar{z}^3}. \quad (4.16)$$

For this geometry, the free stream velocity is given by $U = C(3L^2\bar{x})^{1/3}$ and the velocity field distribution is defined as, $u(x, z) = \frac{\partial\psi}{\partial\bar{z}}$.

The resulting set of equations can be solved by utilization of the required boundary conditions, such as a prescribed velocity profile from the outlet of the torch to the no slip condition on the substrate surface. These boundary conditions are exhibited in the following table.

Boundary	Axial Velocity Component	Radial Velocity Component
$z=L$	$u = \rho_o u_o / 2$	$v=0$
$z=0$	$u=0$	$v=0$

TABLE 4.1 Boundary conditions for the stagnation flow geometry

4.4.2 Development of the Boundary Layer

The redirection of the fluid flow from the stagnation point outward in the radial direction, allows one to simplify the flow to calculate the boundary layer over the substrate. This formulation can be approximated similarly to the Blasius solution. In order for this approximation to be valid, the upstream edge must be sufficiently far away such that, $V_e x_0/\nu \gg 1$, which means the flow must have sufficient time to become fully developed. Utilization of a similarity solution is essential in this case for development of the fluid boundary layer. The formulation for this situation is defined in Fluid Mechanics by Kundu and Cohen³⁵, where the governing equations become,

$$\frac{\partial \psi}{\partial z} \frac{\partial^2 \psi}{\partial r \partial z} - \frac{\partial \psi}{\partial r} \frac{\partial^2 \psi}{\partial z^2} = r \frac{\partial^3 \psi}{\partial z^3}, \quad (4.17)$$

defined by the following boundary conditions

$$\frac{\partial \psi}{\partial z} = \psi = 0 \text{ at } z = 0, r > 0,$$

$$\frac{\partial \psi}{\partial z} \rightarrow V \text{ as } \frac{z}{\delta} \rightarrow \infty.$$

This results in the fluid boundary layer being defined as shown in Eq. 4.18 and the boundary layer thickness for the boundary layer velocity to achieve 99% of the free stream velocity is given in Eq. 4.19.

$$\delta = \sqrt{\frac{\nu x}{V}} \quad (4.18)$$

$$\delta_{99} = 4.9\delta \quad (4.19)$$

This boundary layer thickness is coupled along with the thermal boundary layer discussed in the upcoming sections to help determine the thermodynamic and transport properties within the layer that govern the particle nucleation.

4.5 Energy Analysis (Convection)

The heat transfer over the substrate reduces down to Newton's law of cooling as given below and is used to develop the convection heat transfer coefficient.

$$\left[-k \frac{\partial T(\bar{x}, \bar{z}=0)}{\partial \bar{z}} \right] \frac{r}{L} = h(T_{\text{substrate}} - T_{\infty}), \quad (4.20)$$

where numerical correlations by Martin³⁶ supplies a coherent understanding of the heat transfer coefficient as a function of torch diameter (D_{torch}) and substrate-torch gap (h_{s-t}).

$$\overline{Nu} = \frac{D_{\text{torch}}}{r} \left[\frac{1 - 1.1 D_{\text{torch}}/r}{1 + 0.1 (h_{s-t}/D_{\text{torch}} - 6)^{D_{\text{torch}}/r}} \right] \left[2Re^{1/2} \left(1 + Re^{0.55}/200 \right)^{0.5} \right] Pr^{0.42}. \quad (4.21)$$

The Nusselt number can be used to define the average heat transfer coefficient by

$$\overline{Nu} = \bar{h} D_{\text{torch}} / k. \quad \text{This expression is only valid for } 2 \times 10^3 \leq Re \leq 4 \times 10^5, 2.5 \leq r/D_{\text{torch}} \leq$$

7.5 and $2 \leq h_{s-t} / D_{\text{torch}} \leq 12$.

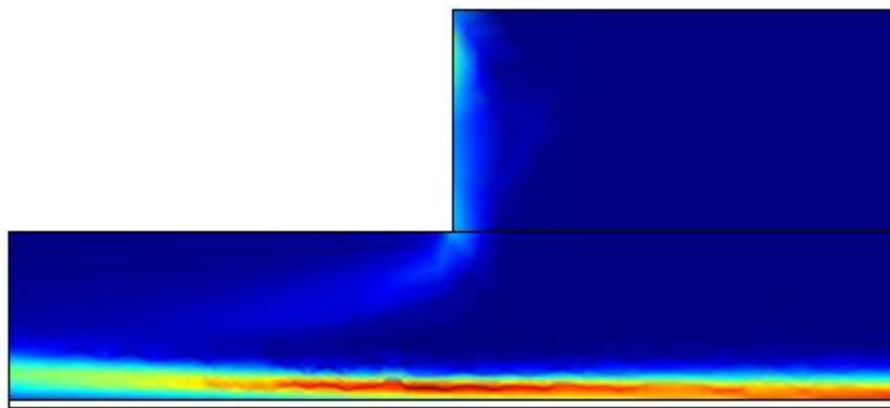


Figure 4.1 Image showing the axial symmetric temperature gradient within the flow approaching the substrate.

In the figure above, the experiment geometry has been simplified by axial symmetry for a case utilizing a plasma temperature of 5500K. The temperature gradient is subtle within the regions immediately exiting the torch, but as the particles approach the substrate they undergo a high degree (>100K/mm) of quenching.

4.6 Species Concentration

From Fick's Law, the diffusion of a species across the fluid boundary layer is calculated to be

$$J_A = -\frac{D_{AB}}{RT} \frac{dc_A}{dr}, \quad (4.22)$$

where J_A is the diffusion flux of species A, c_A is the species concentration of A and D_{AB} is the diffusion constant for species A into B. The species diffusion equation for all species within the chemical reaction becomes

$$2U \frac{dY_k}{d\bar{z}} + \frac{d}{d\bar{z}}(\rho Y_k U_k) - W_k \dot{\omega}_k = 0. \quad (4.23)$$

Where U_k is defined as the diffusion velocity of the k^{th} species, W_k is the molar mass and $\dot{\omega}_k$ is the molar ratio of production for the chemical reactions of the k^{th} species. From the species diffusion equation, the species concentrations at various axial locations can be determined. Approximation of the concentration gradient can be defined by

$$\frac{dc_A}{d\bar{x}} \cong \frac{\Delta c_A}{\Delta \bar{x}} = \frac{c_{AB} - c_{A,S}}{\delta}, \quad (4.24)$$

which is the ratio of the flow to surface species concentration difference to the boundary layer thickness.³⁷

Chapter 5

Synthesis of Cubic Boron Nitride

Cubic boron nitride production as seen in the literature is typically produced by high-temperature, high-pressure techniques and generally contain large grain sizes. Synthesis by thermal plasma gives a wide manipulation range of key processing parameters such as temperature and residence time to reduce this grain size. These parameters are inter-related and need to be addressed individually to fully evaluate their relationship with the phase produced and the particle agglomeration.

5.1 Temperature Effect

5.1.1 Parameter Space

To evaluate the effect of the temperature on c-BN growth, a series of experiments were conducted where a fixed residence time was implemented, while plasma temperature was varied. RF power was varied between 500W and 1400W in 100W increments, which results in temperatures ranging from 3000K and 8500K. The residence time set consisted of durations from 0.005s to 0.08s in .005s intervals. Effectively each residence time set investigated a range of temperatures, through which the average percentage of cubic phase with respect to plasma temperature is given in the following section.

5.1.2 Results and Discussion

The synthesis of c-BN by thermal plasmas requires extreme temperatures to adequately create a super-saturation such that powders homogeneously nucleate out of the flow field. From the conducted experiments, one can observe the percent cubic phase increasing rapidly with plasma temperature up to 6500K. The most extreme temperatures of those explored in this work yielded an increasing amount of hexagonal boron nitride. This is believed to be due to the particles undergoing annealing on the substrate, which is induced by the excess temperatures approaching the stagnation point during the ten minute long experiments. Other temperatures have produced significant percentages of the cubic phase, but the residence time must be adjusted accordingly.

It is worth noting that the total residence time is composed of both precursor decomposition and subsequent particle growth. The precursor decomposition time should be sufficiently long for complete conversion of the precursor species; and the subsequent particle growth time should be sufficiently long for crystallization into the cubic phase, while short enough to quench the particle in the cubic phase. Optimization of the residence time involves properly controlling both the mass flow rate (for particle velocity) and the distance between the torch and substrate. The following results are for the total residence time, which includes both effects.

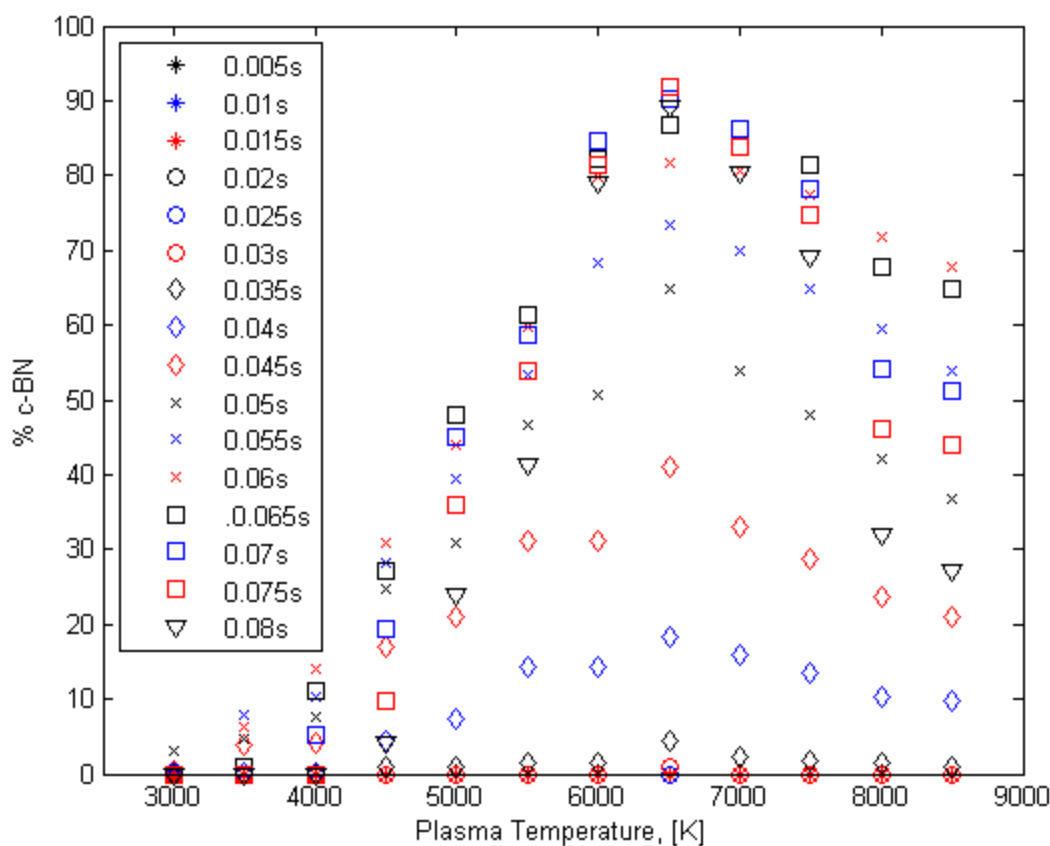


Figure 5.1 Plot of the percentage of cubic phase as a function of plasma temperature for different residence times.

As shown in Figure 5.1, the cubic structure of boron nitride does not form in high percentages at relatively low temperatures. At the lower plasma temperatures, the cubic phase is overwhelmed by amorphous boron nitride and the hexagonal phase. Increasing the plasma temperature has led to observations of the formation of c-BN being a nonmonotonic function of temperature (with a local maximum), but the decrease in purity at higher temperatures is believed to be due to annealing of the powder on the substrate. This results in the cubic phase being an increasing function of temperature because the particles have sufficient energy to rearrange the crystal lattice into the cubic structure. Also, from this plot, one can observe that the phase composition is a strong function of

residence time, showing a continuous increase in c-BN growth with increasing dwell time.

Relatively low plasma temperatures, between 3000K and 4000K, yielded a very poor percentage of c-BN nanopowder. At a temperature of 3000K, there was only one residence time explored that resulted in any traces of cubic phase, which was a dwell time of 0.05s. This is believed to be the optimal dwell time for this temperature, and has resulted in a powder composed of approximately 4% cubic structure. As the plasma temperature is increased to 4000K, the maximum cubic composition increased to nearly 15%. The optimal residence time also increased, as seen in Figure 5.1, with the plasma temperature to 0.06s.

As the plasma temperature increases to the range between 4500K and 5500K, the possible residence times that yield any cubic phase becomes broader. Observations of the desired phase produced from a plasma at 4500K, is discovered in the range of 0.035s - 0.08s. Further increasing the temperature to 5500K exhibited c-BN growth at similar durations, but this showed a significantly higher yield of cubic phase in the as-synthesized powder. Nanopowders produced at 5500K and 0.065s resulted in approximately 60% cubic phase. The limits of cubic formation, for the 5500K case, were observed at 0.035s and 0.08s, where the powders were ~1.5% and ~40% c-BN, respectively. The maximum cubic composition, for this case, is more than double that of the 4500K case and the optimal residence time was shifted by 0.005s.

The highest percentages of cubic phase were observed from experiments with plasma temperatures in the range between 6000K and 7000K. Nanopowders synthesized at 6500K displayed the highest c-BN content throughout the dwell time range. The

maximum percentage, approximately 93%, occurred at a residence time of 0.075s. Also, at this temperature, the onset of cubic boron nitride formation occurred at a residence time of 0.030s, which is 0.005s shorter than any other case in the experiment set. As the plasma temperature increased above 6500K, as seen in the 7000K case, the cubic phase percentage begins to decrease. The most drastic decrease is observed in the 0.08s case, of which the powder composition contained ~10% less cubic phase less than the 0.075s case.

Increasing the plasma temperature above the optimum, 6500K, results in a dramatic decrease in cubic content. In the range of 7500K and 8500K, the overall cubic content rapidly decreases across the residence time range. The maximum c-BN content, under a given residence time of 0.065s, decreases nearly 15% from ~84% to ~69% for 7500K and 8500K, respectively. The first occurrence of c-BN has shifted under higher temperatures to 0.035s; this is a 0.005s increase from the 6500K case. At longer residence times, these extreme temperatures cause a loss of cubic phase. This is most likely due to the substrate overheating, which causes the particles to become annealed on the substrate, converting these particles from cubic to hexagonal phase. Overheating of the substrate is most noticeable in the 8500K case because of the large decrease in the percentage of c-BN from the 0.08s experiment. The experiments conducted, in the temperature range between 7500K – 8500K, yielded a decrease of over 40% c-BN content at the longest residence time.

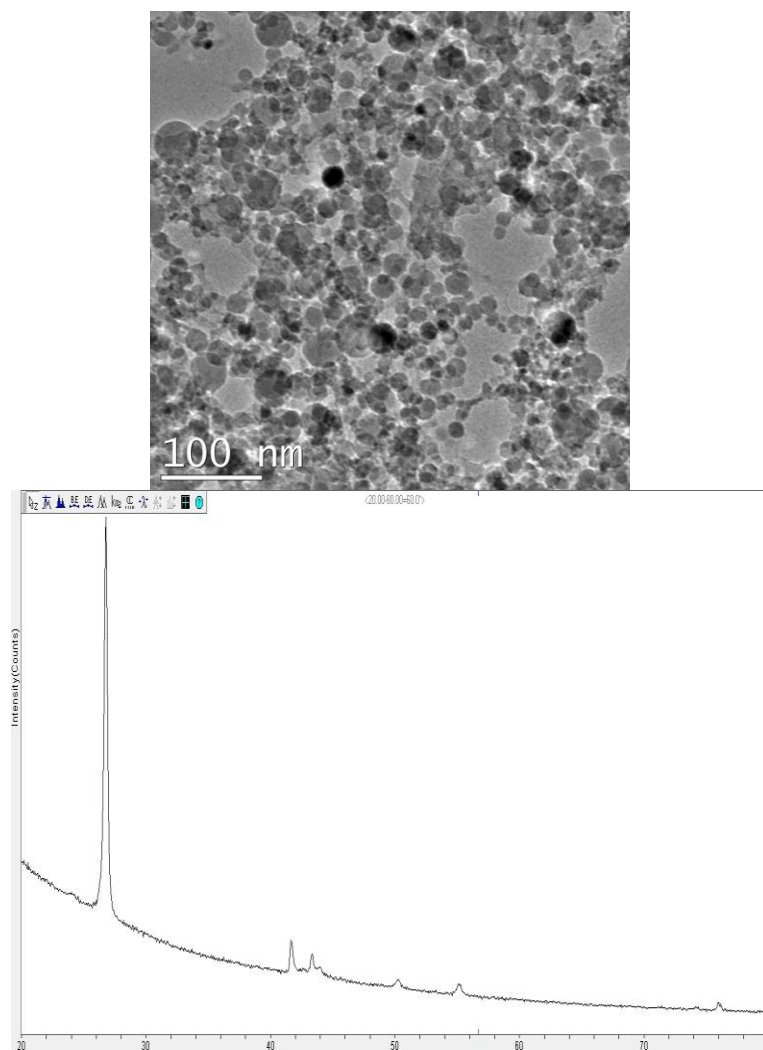


Figure 5.2 XRD and TEM of powder synthesized from an ICP at 4000K and 0.065s.

Above, in Figure 5.2, are the XRD and TEM images from a BN nano-powder sample synthesized at a plasma temperature and dwell time of 4000K and 0.065s. As seen in the XRD scan, this powder is composed of nearly pure hexagonal boron nitride, with minimal c-BN content. The main impurity in the sample is a resultant of the substrate, which is aluminum. From TEM, the particle morphology was observed to be spherical with an average particle size of ~20nm. These particles ranged from ~5nm to ~50nm in diameter. The wide range of particle size is due to the time-temperature profile of each particle being not completely uniform in the radial direction.

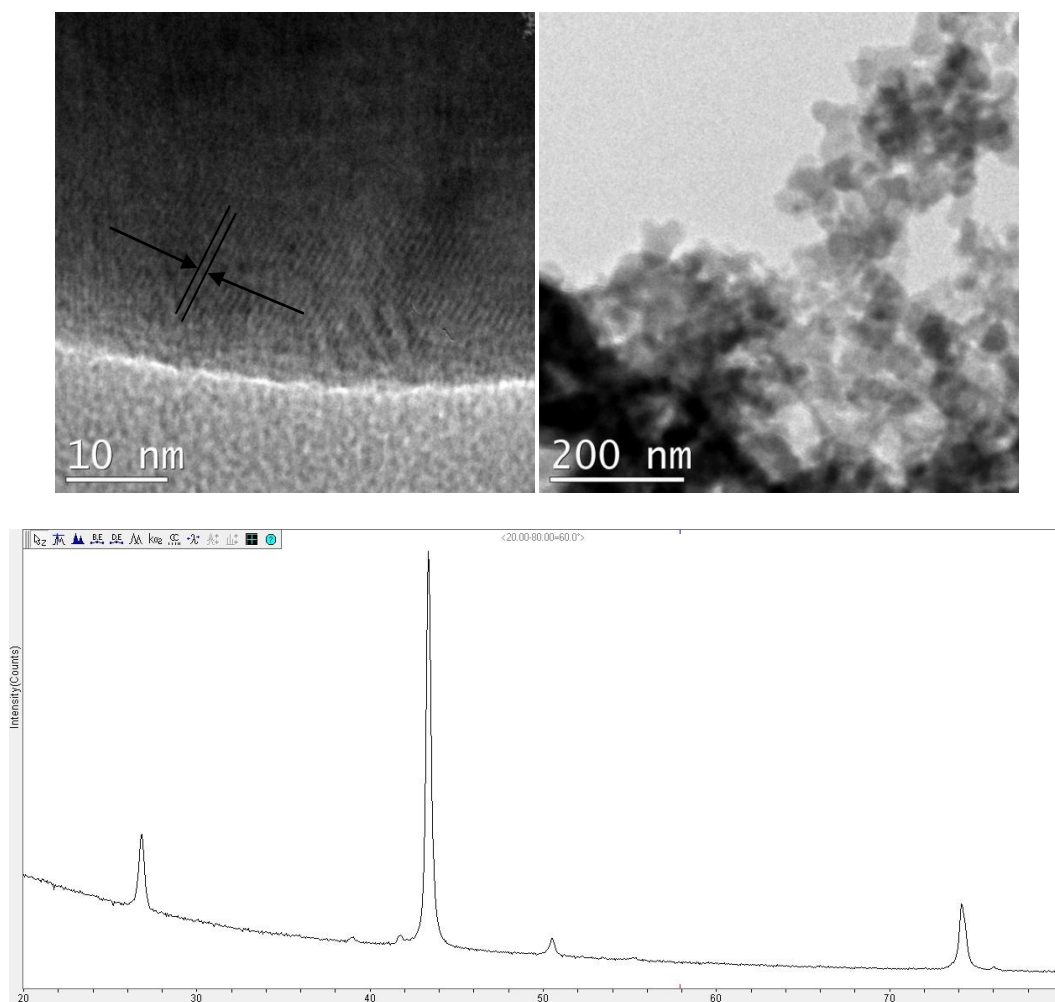


Figure 5.3 (a) HRTEM and (b) TEM images (c) XRD of c-BN particles formed from a plasma temperature of 6500K.

The HRTEM and TEM images displayed in Figure 5.3 (a) and (b) exhibit the crystal lattice spacing, particle morphology, and average particle size, respectively. From Figure 5.3 (a), the crystal lattice parameter is $a=3.625\text{\AA}$, which matches the c-BN lattice dimension given in the JADE database for the (111) growth plane. The particles of cubic structure are more faceted, while the spherical morphology is the hexagonal particles. From Figure 5.3 (b), the average particle size is approximately 50nm with a very narrow

size distribution. This powder was synthesized at 0.06s and 6500K, which resulted in ~82% cubic structure as seen in the XRD image Figure 5.3 (c).

The TEM diffraction patterns, shown below in Figure 5.4 (a) and (b), give an insight into the structures present within powder manufactured at 0.03s and 6500K. From the faint diffraction rings in Figure 5.4 (a), one can conclude there are sections of purely amorphous particles. On the other hand, Figure 5.4 (b) displays a particle mixture with d-spacings resembling a polycrystalline material.

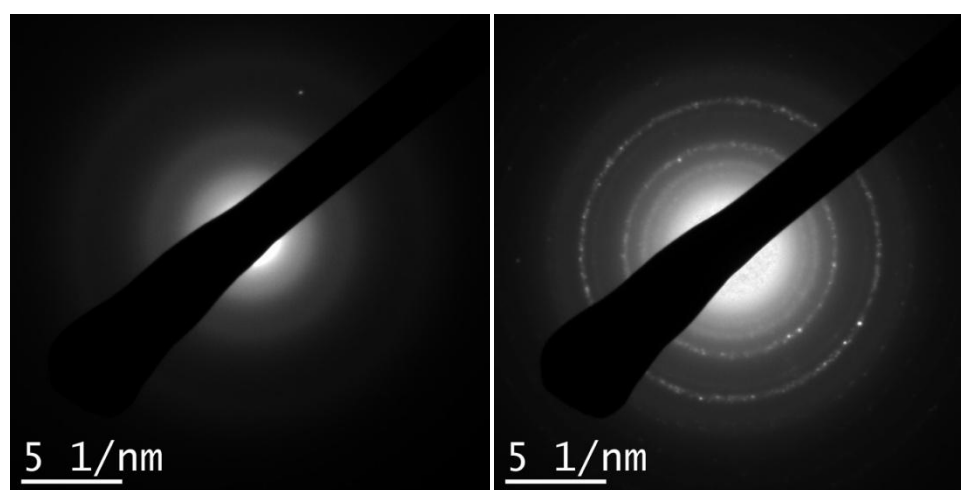


Figure 5.4 TEM diffraction patterns of (a) amorphous and (b) a hexagonal/cubic boron nitride mixture.

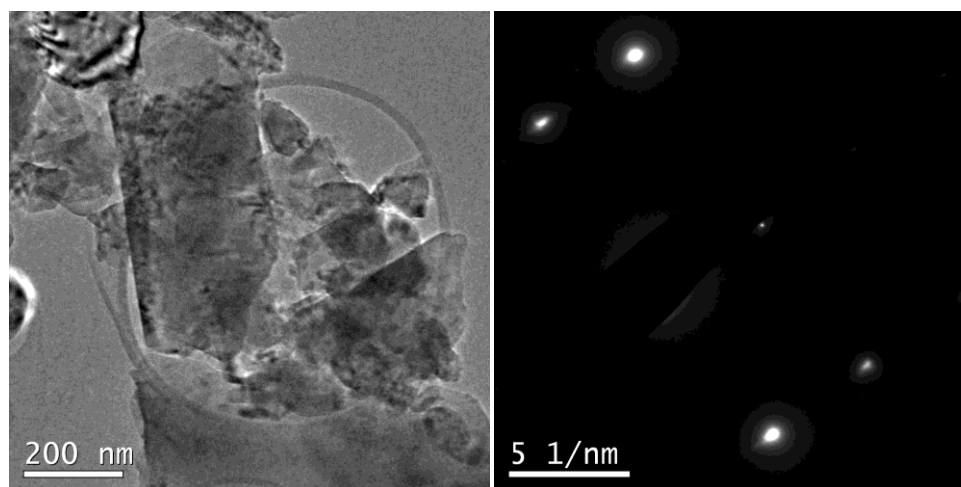


Figure 5.5 TEM image and diffraction pattern of c-BN particles synthesized at a plasma temperature of 7500K and a decomposition time of 0.075s.

As seen from the series of TEM images and diffraction patterns displayed in this study, the lattice structure is a strong function of plasma temperature as well as residence time. As plasma temperature increases, the c-BN content also increases with a proportional decrease in the hexagonal structure. From the relationship for particle growth, discussed earlier in this study, the resulting particle sizes when exiting the plasma region are very small, but the resulting mean particle size, as established from the TEM images, are relatively large. Thus the excess particle growth must be from post plasma particle-particle interactions.

5.2 Residence Time Effect

5.2.1 Parameter Space

To evaluate the effect of the residence time on c-BN growth, a series of experiments were conducted where a fixed synthesis temperature was implemented, while residence time was varied. RF power was varied between 500W and 1400W in 100W increments, which results in residence times ranging from 0.005s to 0.08s. The synthesis temperature set consisted of temperatures from 3000K and 8500K in 500K intervals. Effectively each temperature set investigated a range of residence times, through which the average percentage of cubic phase with respect to plasma temperature is given in the following section.

5.2.2 Results and Discussion

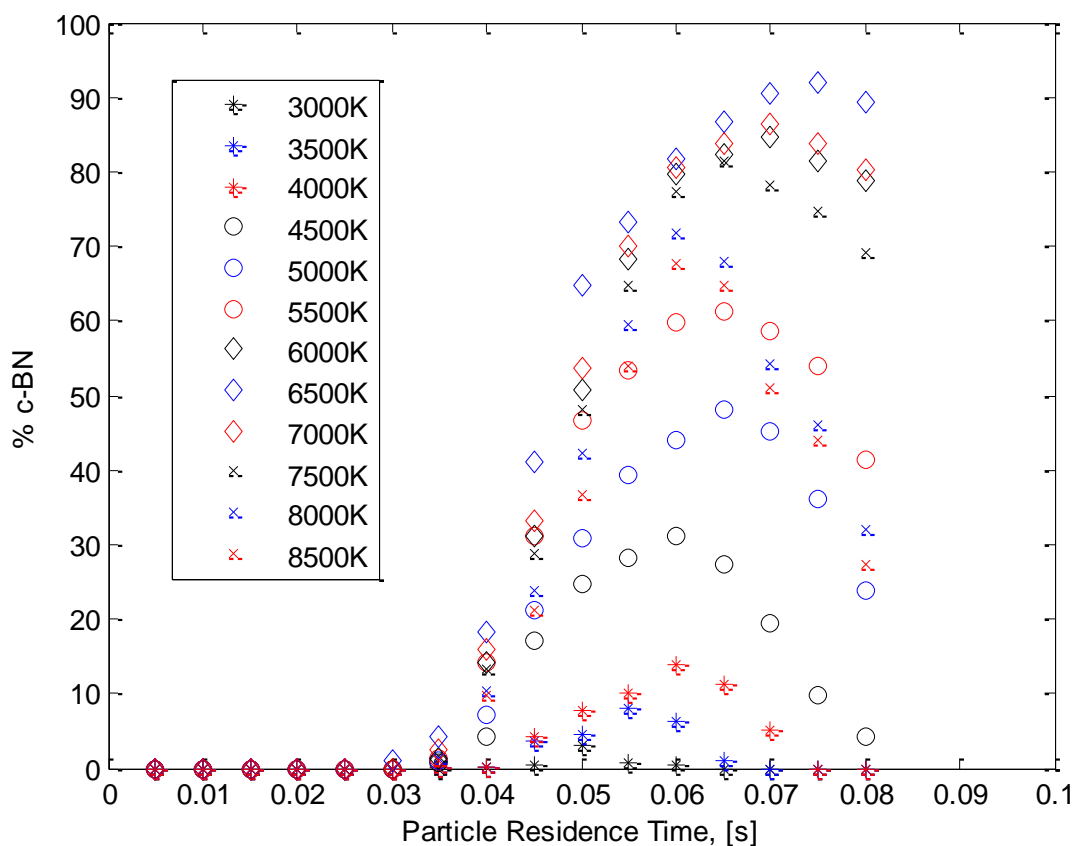


Figure 5.6 Percent cubic phase as a function of residence time.

As shown in Figure 5.6, the cubic structure of boron nitride does not form during short residence times. This is believed to be due to insufficient time for particle interactions to occur. Increasing the residence time has led to observations of the formation of c-BN being a nonmonotonic function of residence time. Also, from this plot, one can observe the residence time, at which the maximum percentage of cubic phase occurs is shifted to longer durations as the plasma temperature increases.

Shorter residence times, between 0.005-0.04s, yielded little or no c-BN nanopowder. During experiments conducted in this range, it was observed that the onset of cubic structure formation occurred at 0.03s by plasma operating at 6500K. 3000K case

resulted in no traces of cubic phase, except at a decomposition time of 0.05s. This is believed to be the optimal residence time (for the 3000K set) and has resulted in a powder composed of approximately 4% cubic. During the 4000K set, the maximum cubic composition increased to ~15% at a residence time of 0.06s.

As the plasma temperature increases to the range between 4500K and 5500K, the possible residence times that yield any cubic phase becomes broader. The desired phase produced from a plasma at 4500K, was observed at residence times as short as 0.035s and as long as 0.08s. Nano-powders produced at 0.65s resulted in a maximum of approximately 60% cubic, while the temperature was held at 5500K. The limits of cubic formation, for the 5500K case, were observed at 0.035s and 0.08s, where the powders were ~1.5% and ~40% c-BN, respectively.

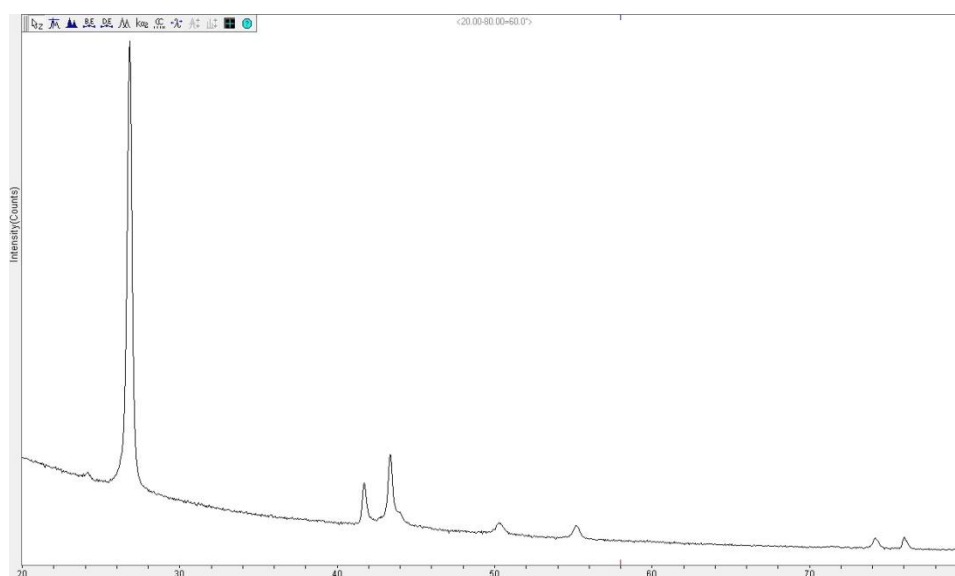


Figure 5.7 XRD spectrum of a c-BN/h-BN powder composition synthesized at 0.04s and 5000K.

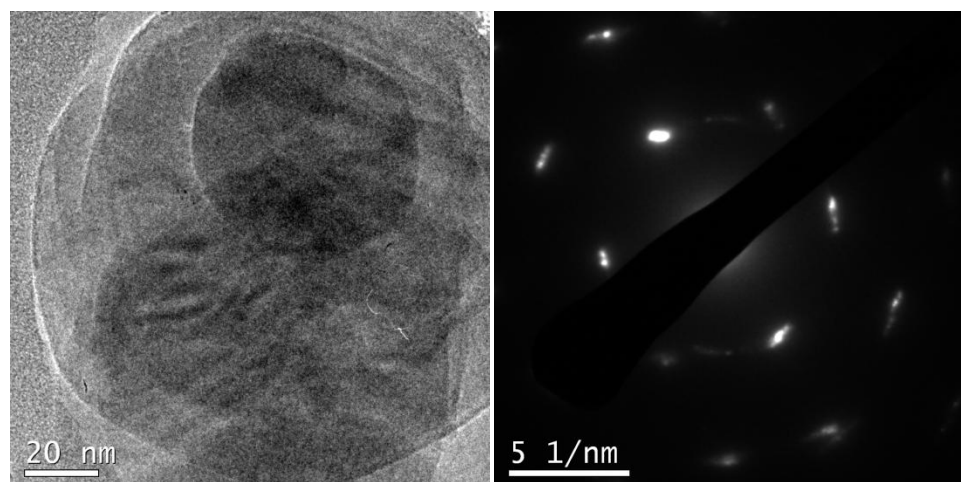
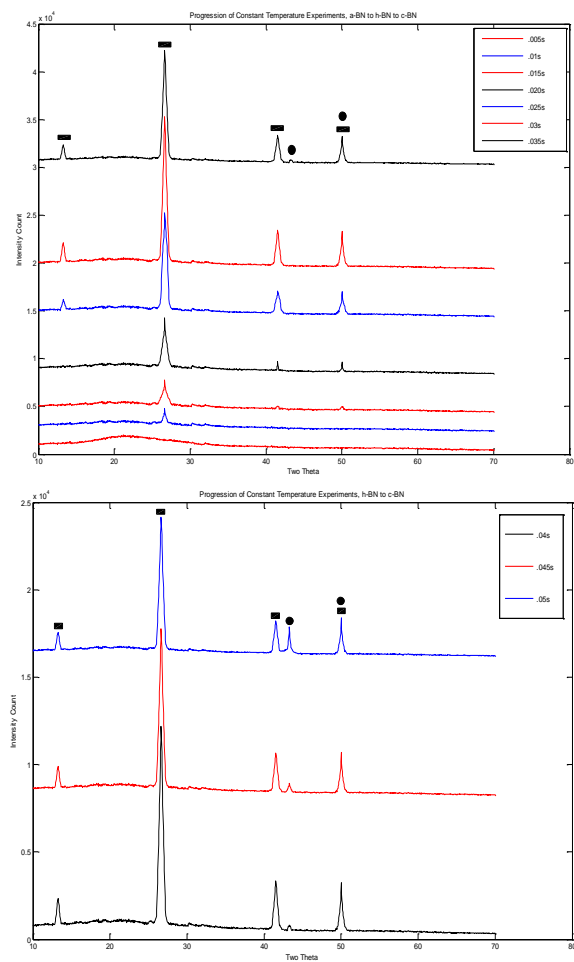


Figure 5.8 (a) Highly agglomerated hexagonal structured nano-particle (b) Hexagonal structure diffraction pattern.

From the figures above, the 8% cubic phase nanopowder formed at 0.04s and 5000K was observed to be formed of highly agglomerated particles. This is shown in Figure 5.8(a) by the close proximity of ~25nm radii particles in relation to the ~60nm radii particles. This sample was sonicated for 48 hours and re-examined, but the agglomerations were still present.

The highest percentages of cubic phase were observed from experiments with plasma temperatures in the range between 6000K and 7000K. Nano-powders synthesized at 6500K displayed the highest c-BN content throughout the residence time range. The maximum percentage, approximately 91%, occurred at a residence time of 0.075s. Also, at this temperature, the onset of cubic boron nitride formation occurred at a residence time of 0.030s, which is 0.005s shorter than any other case in the experiment set. As the plasma temperature increased above 6500K, as seen in the 7000K case, the cubic phase percentage begins to decrease. The most drastic decrease is observed in the 0.08s residence time case, of which the powder composition contained ~10% less cubic phase.



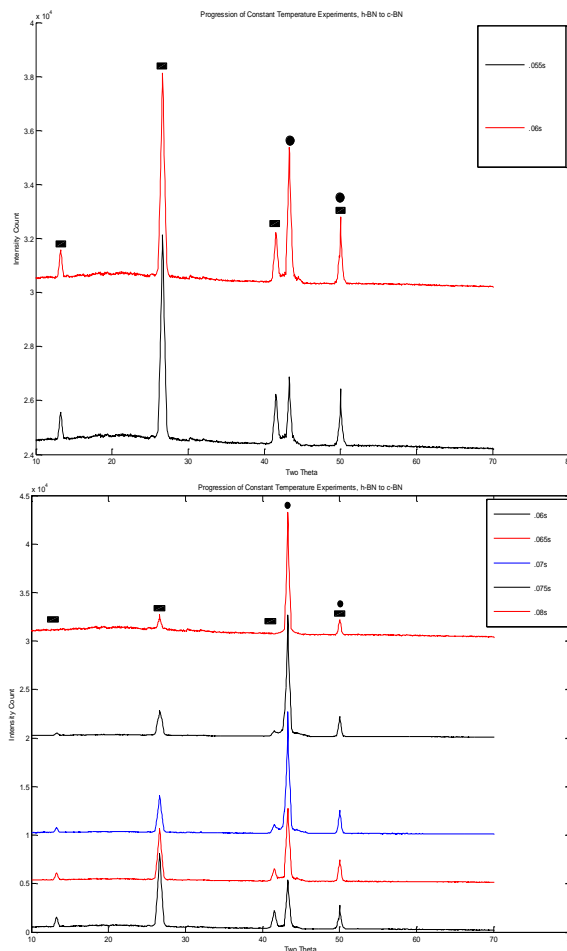


Figure 5.9 (a) Crystal growth from amorphous particle to h-BN (b) Onset of c-BN growth to increasing c-BN content (c) Nano-powders with majority c-BN content (d) Powders with >80% cubic phase.

XRD scans of powders synthesized from a plasma temperature of 6432K with a residence time range between 0.005s and 0.08s are shown in Figure 5.9a, b, c, and d. The powders formed at shorter residence times resulted in a mainly amorphous structure. This is due to the particles not having sufficient time to rearrange into any long range order. As the residence time increases, the crystal lattice reverts to a hexagonal structure, until the first observation of cubic phase at 0.035s. The powders at lower residence times were a majority of hexagonal because of the particles having insufficient time for densification. The content of c-BN rapidly increases as the residence time increases to

0.075s, which the maximum is ~91%. This determines the optimal residence time to be 0.075s for this plasma temperature.

Increasing the plasma temperature above the optimum, 6500K, yields in a dramatic decrease in cubic content. In the range of 7500K and 8500K, the overall cubic content rapidly decreases across the residence time range. The residence time, at which these maximum content powders were synthesized, also shift to shorter durations by 0.005s from 0.065s to 0.06s. The first occurrence of c-BN has shifted at higher temperatures to 0.035s; this is a 0.005s increase from the optimum temperature observed previously. At longer residence times, these limit temperatures cause a loss of cubic phase. This is most likely due to the particles having sufficient time at elevated temperatures to create atomic mobility and form the equilibrium structure, which is the hexagonal structure.

Below, the 0.075s and 7500K case is shown, by XRD, to consist of 75% cubic phase. The particles formed under these conditions were observed by TEM to have a preferential growth direction as displayed in Figure 10a by the faceted morphology. The faceted morphology is believed to occur during post-deposition onto the aluminum substrate because there is no flow-field route that would result in gas phase preferential growth. This is due to overheating of the substrate from the extreme plasma temperature, which created coalescence between c-BN particles forming larger faceted structures. The phenomenon also explains the increase in hexagonal phase, which is explained to occur due to the increase in atomic mobility to reconfigure the crystal structure. Atomic mobility within the particles occurs post coalescence.

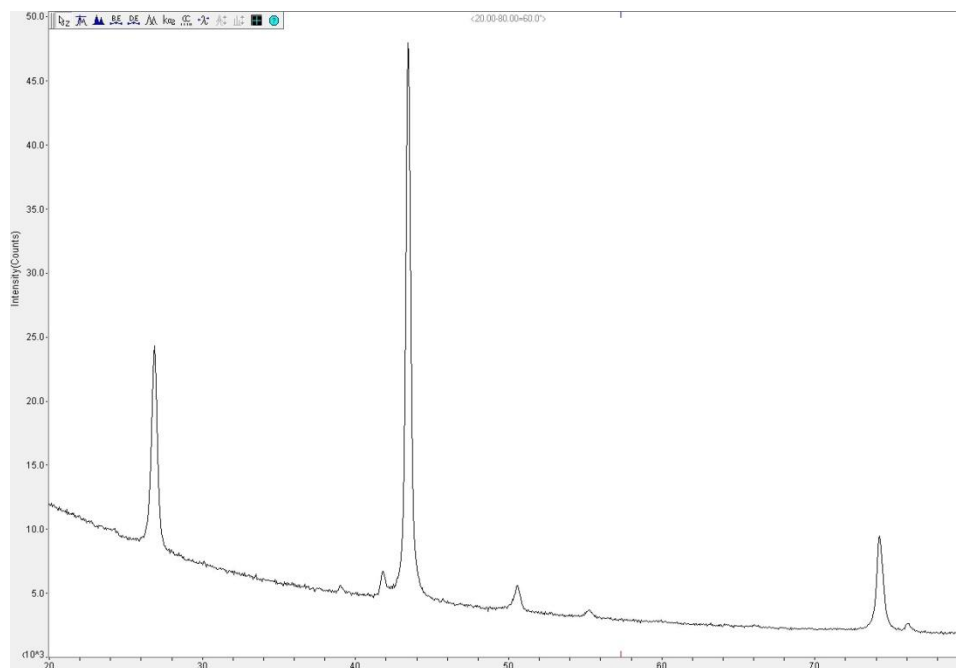


Figure 5.10 XRD of as-synthesized nanopowders formed at 0.075s and 7500K.

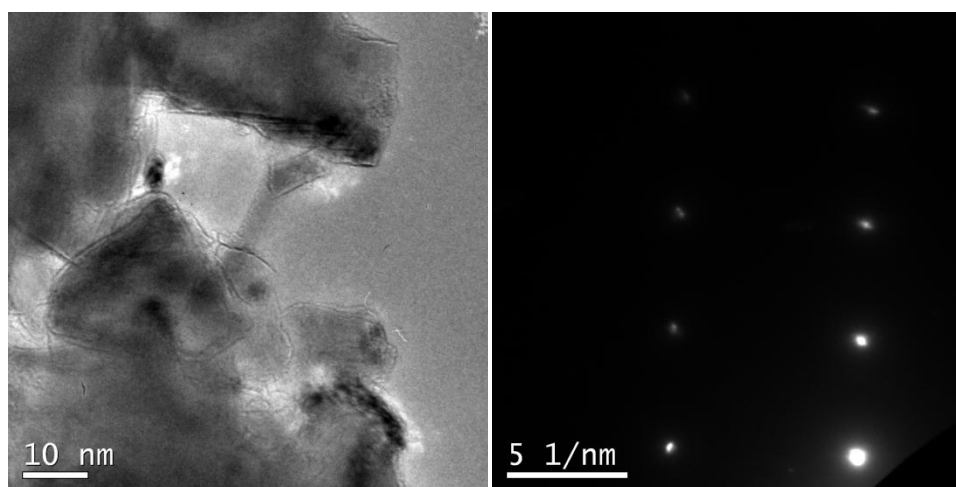


Figure 5.11 (a) TEM image and (b) diffraction pattern of the 0.075s and 7500K case.

HRTEM of nano-particles is shown in Figure 5.12 (a) and (b). These particles were synthesized at plasma conditions of 0.075s and 6500K, for residence time and temperature, respectively. Two separate particles from different regions of the sample were probed to display the lattice spacing. The lattice spacing in both images match

exactly to the lattice parameter of 3.625\AA given in the JADE database for cubic boron nitride.

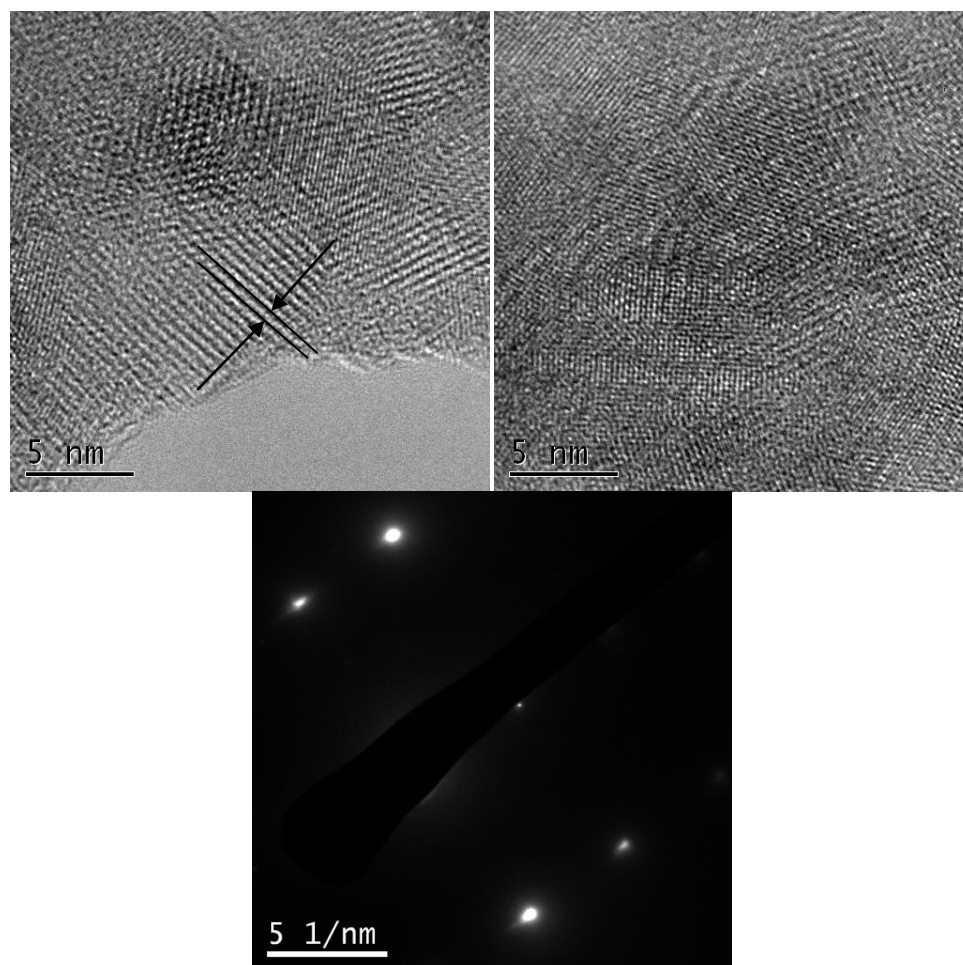


Figure 5.12 (a) and (b) HRTEM images and (c) diffraction pattern of c-BN particles synthesized at a plasma temperature of 6500K and a residence time of 0.075s.

Chapter 6

Concluding Remarks

6.1 Review of Results

In this work, growth mechanisms such as plasma temperature and residence time of c-BN nanostructured powders were investigated. Aerodynamically-enhanced inductively-coupled plasma was implemented to perform parametric studies on the growth mechanisms involved in the synthesis of c-BN nanopowders. A single source precursor, borane ammonia, was utilized to manufacture cubic boron nitride. The experimental conditions conducted within this study were chosen by the limiting cases of the apparatus. Temperature of the plasma was varied between 3000K and 8500K, which the lower limit was selected for the minimum plasma temperature to decompose the precursor in-situ and the upper limit is due to the thermal property limitations of the quartz torch. Residence time, which was defined as the duration for the feed particles to travel through the plasma region, was varied between 0.005s and 0.08s. The as-synthesized nano-powders were characterized by TEM and XRD to obtain information on composition and mean particle size. The above stated experiment sets enabled an analysis to develop an understanding for c-BN growth conditions.

Experiments to exploit the effect of plasma temperature on the formation of cubic phase were performed by conducting given residence time cases. This developed an explicit relationship between these two parameters. The purity of the synthesized c-BN powder is a parabolic function of temperature. Most cases conducted exhibited the

maximum percentage of cubic phase at a plasma temperature of 6500K. Plasma temperatures below 6500K displayed mixed phases of amorphous, hexagonal and cubic structures. As the residence time increases, the percentage of cubic phase present in the powder increases at all plasma temperatures in the experiment set. This is believed to be due to the longer durations giving more time for precursor decomposition and for the crystalline structure to evolve.

Constant temperature cases were developed to determine the percentage of c-BN formed as a function of residence time. Trends have shown optimal durations for synthesizing cubic phase at each temperature within the experimental range. At relatively low plasma temperatures, there were no durations that yielded cubic structure formation. As the plasma temperature increased, the particle interactions sway towards favorable conditions to realign the molecular structure into a cubic unit cell. The optimal residence time varied from case to case in a linearly increasing relationship from 3000K to 6500K. Plasma temperatures exceeding this temperature of 6500K resulted in lower purity powders (up to ~40% less in the 0.08s case), which are believed to be due to the annealing of the particles on the substrate.

6.2 Future Work

Several improvements must be made within the knowledge of the physical chemical kinetics producing the various phases of boron nitride. This should be done by taking axial scans of the flow field using various techniques such as Raman Spectroscopy, Laser Induced Fluorescence and Particle Image Velocimetry. These techniques will enable probing for species concentrations, temperature distribution and velocity distribution as a function of the axial direction, respectively. The current

methods used are similar to a black-box technique in the way that the inputs and outputs are known, but there is very limited information about the kinetics between these points. In gas phase synthesis of nano-powders, it is imperative to have such experimentations.

Experiments to expand the group's knowledge of conditions favorable for synthesis of the cubic structure include varying the substrate-torch gap, temperature of the substrate, and argon concentration. Varying the substrate will give the ability to investigate the post-plasma residence time effect, which will supply information on possible chemical reactions in the flow field as well as how this affects particle growth. Performing a series of experiments where the substrate is adjusted between two temperature extremes will provide data to explain definitively whether the substrate can reach a temperature high enough to create atomic mobility as to change the crystalline structure from cubic to hexagonal. And finally, investigating the relationship between argon concentration and the percentage of cubic phase observed in the as-synthesized powder will enable the group to determine if excess argon hinders particle formation and growth by limiting BN particle interaction.

References

- ¹ Zhao, Hong, PhD, Rutgers The State University of New Jersey – New Brunswick, 2007
- ² DJ Kester, RJ Messier, *Journal of Applied Physics*, 72 (1992) 504-513
- ³ C. Ronning, *APPLIED PHYSICS A: MATERIALS SCIENCE & PROCESSING*. Volume 77, Number 1, 39-50, DOI: 10.1007/s00339-002-2063-7
- ⁴ J Robertson, *Diamond and Related Materials*, 5 (1996) 519-524
- ⁵ MP Chowdhury, AK Pal, *Journal of Applied Physics*, 37 (2004) 261-268
- ⁶ DR McKenzie, WD McFall, WG Sainty, CA Davis, RD Collins, *Diamond and Related Materials*, 2 (1993) 970-976
- ⁷ J Robertson, *Pure and Applied Chemistry*, 66 (1994) 1789-1796
- ⁸ W Dworschak, K Jung, H Ehrhardt, *Thin Solid Films*, 254 (1995) 65-74
- ⁹ DR McKenzie et al. *Surface and Coating Technology*, 78 (1996) 255-262
- ¹⁰ H Hofsäss, H Feldermann, M Sebastian, C Ronning, *Physical Review B: Amer. Phys. Soc.* 55 (1997) 13230-13233
- ¹¹ DH Burns, MA Cappelli, *Applied Physics Letters* 68 (1996)
- ¹² K Larsson, *Thin Solid Films*, 515 (2006) 401-406
- ¹³ A Bartl et al. *International Journal of Refractory Materials* 14 (1996) 145
- ¹⁴ H Uchida, M Yamashita, S Hanaki, A Kurihara, *Materials Science and Engineering A*, 483-484 (2008) 695-697
- ¹⁵ H Yamamoto, S Matsumoto, K Okada, J Yu, K Hirakuri, *Diamond and Related Materials*, 15 (2006) 1357-1361
- ¹⁶ J Ye, H Oechsner, *Thin Solid Films*, 514 (2006) 138-144
- ¹⁷ DJ Kester, R Messier, *J. Applied Physics*, 72 (1992) 504-513
- ¹⁸ M Murakawa and S Watanabe, *Surf. Coatings Tech.* 43-44 (1990) 128-136
- ¹⁹ T Yoshida, *Diamond and Related Materials*, 5 (1996) 501-507
- ²⁰ I Konyashin, J Loeffler, J Bill, F Aldinger, *Thin Solid Films* 101 (1997) 308-309
- ²¹ T Watanabe, R Sataka, K Yamamoto, *Thin Solid Films* 516 (2008) 4462-4467
- ²² T Kawamoto et al. *Review of Scientific Instruments* 75 (2004) 2451-2454
- ²³ T Werninghaus et al. *Diamond and Related Materials*, 6 (1997) 612-616
- ²⁴ J Guo et al. *Electrochemistry Communications*, 9 (2007) 1824-1827
- ²⁵ JM Hollander, WL Lolly, *Acc. Chemical Research* 3 (1970) 193-200
- ²⁶ High technology ICP torch tube. 4 October 2011. <http://sgmdz.en.alibaba.com/product/419566228-212728239/High_technology_ICP_torch_tube.html>
- ²⁷ Lieberman, Lichtenberg (2005). *Principles of Plasma Discharges and Materials Processing*. Second Edition, New York: John Wiley and Sons, Inc.
- ²⁸ http://www.lexellaser.com/techinfo_gas-ion.htm
- ²⁹ Moeck, P. X-ray Diffraction. 4 October 2011. <web.pdx.edu/~pmoeck/phy381/Topic5a-XRD.pdf>
- ³⁰ TOPCON 002B. 4 October 2011. <www.technicalsalesolutions.com/items.php?CID=4>
- ³¹ Matsoukas, T., Russell M. (1995), *J. Appl. Phys.* 77, 4285.
- ³² Matsoukas, T., Russell, M., Smith, M. (1996), *J. Vac. Sci. Technol.* A14, 624.
- ³³ Boufendi, L., Plain, A., Blondeau, J.P., Bouchoule, A., Laure, C., Toogood, M. (1992), *Appl. Phys. Lett.* 60, 169.
- ³⁴ Hollenstein, Ch., Schwarzenbach, W., Howling, A. A. , Courteille, C., Dorier, J.-L., Sansonnens, L., *Jour of Vac Science & Tech A: Vacuum, Surfaces, and Films*, 14 (1996) 535-539.
- ³⁵ Kundu, P.K., Cohen, I.M. (2004). *Fluid Mechanics*. Third Edition. San Diego: Elsevier Academic Press.
- ³⁶ Burmeister, L.C. (1993). *Convective Heat Transfer*. Second Edition. Hoboken: John Wiley and Sons, Inc.
- ³⁷ Memon, N. MS., Rutgers The State University of New Jersey – New Brunswick, 2009.